

A phenomenological hardening model for an aluminium-lithium alloy

Niraj Nayan^{a,b}, Sivasambu Mahesh^{c,*}, M. J. N. V. Prasad^b,
S. V. S. N. Murthy^a, Indradev Samajdar^b

^a*Vikram Sarabhai Space Centre, Trivandrum 695022. India.*

^b*Department of Metallurgical Engineering & Materials Science,
Indian Institute of Technology Bombay, Powai, Mumbai 400076. India.*

^c*Department of Aerospace Engineering,
Indian Institute of Technology Madras, Chennai 600036. India.*

Abstract

A phenomenological hardening model based on the extended Voce law is proposed to capture the plastic flow of a third generation aluminium-lithium alloy. The model includes a simple precipitation law, which accounts for pre-ageing plastic deformation, and a hardening law that accounts for the hardening of the matrix, and for the interaction of matrix glide dislocations with anisotropic and isotropic precipitates. Flow stress evolution in solution treated, underaged, and peak-aged samples is measured through uniaxial tensile tests on specimens cut at 0°, 45°, and 90° to the rolling direction. The measured flow stress evolution in all the tempers is captured well by the model. The model parameters offer insights into the sub-structural evolution that accompanies plastic deformation.

Keywords: aluminium-lithium, flow, age-hardening, flow stress, anisotropy

*Corresponding author

Email address: smahesh@iitm.ac.in (Sivasambu Mahesh)

1. Introduction

The strength of precipitate hardened alloys has been extensively studied, going back at least to Mott and Nabarro (1940). It is well-established that these alloys derive their strength from the mechanisms of precipitation strengthening, solution strengthening, grain and sub-grain strengthening, and dislocation strengthening (Starink et al., 1999). Precipitation strengthening itself arises from a combination of order strengthening, dispersion strengthening, stacking fault strengthening, and modulus hardening (Ardell, 1985). Sub-models and expressions for each of these strengthening contributions have been developed in the literature. A number of works, e.g., Shercliff and Ashby (1990a,b), and Starink et al. (1999), have synthesised these sub-models to predict the yield strength of Al-Li alloys as a function of ageing time and temperature.

The yield strength determines the structural integrity of the manufactured components. It can be severely anisotropic in precipitate hardened Al-Li alloys. For example, in a second generation Al-Li alloy sheet, Lee et al. (1999b) report that the ratio of the yield strengths in a direction inclined 45° to the rolling direction (RD), and that along RD is only slightly more than 0.5. Yield strength anisotropy constricts the design envelope of the material. Therefore, much attention has been directed toward understanding its origins and developing means to alleviate it (Huang and Ardell, 1988; Vasudevan et al., 1990; Kim and Lee, 1993; Crooks et al., 1998; Lee et al., 1999b; Garmestani et al., 2001). These studies have established that a large part of the plastic anisotropy can be attributed to the strong brass texture of the material, and the remainder to the inhomogeneous precipitation in crys-

tallographically equivalent habit planes. Progress in alloy design has led to the elimination of the strong brass texture, resulting in substantially reduced yield strength anisotropy in third generation Al-Li alloys (Rioja and Liu, 2012).

Together with yielding, understanding the plastic flow of Al-Li alloys is also important, as manufactured components are subjected to a variety of forming operations in various tempers. The processing route to producing peak aged Al-Li components takes one of two paths, depending on the quantum of plastic deformation required to produce the component in its net or near net shape. If it is necessary to impart only small plastic strains to produce a component in its net or near net shape, the starting material blank may be of PA temper. An example of such a process is roll bending to produce fuel tanks for space applications (Campbell Jr, 2011). However, the peak-aged material is not suitable as the starting material if large plastic strains must be imparted during forming, e.g., in spin forming operations for tanks, or tank domes. This is because the peak aged material lacks sufficient ductility. In this case, the component is formed to near net shape in the solution treated temper, which has higher ductility. The near net formed component is then age hardened to obtain superior strength (Crooks et al., 1998). Understanding the flow response of Al-Li alloys in the solution treated, peak aged, and intermediate underaged conditions is necessary for estimating the forces and pressures required for forming operations.

While the initial yield surface can be well-captured using an analytical function (Choi et al., 2001; Barlat et al., 2003; Kabirian and Khan, 2015), more complex models are required to capture the flow response, i.e., the evo-

lution of the yield surface with plastic deformation (Choi and Barlat, 1999; Rousselier et al., 2009; Safaei et al., 2013; Shi and Mosler, 2013; Yoshida et al., 2015; Cyr et al., 2018). Polycrystal plasticity models, which represent the sub-structural evolution within grains, may be able to predict the flow response. To our knowledge, a model capable of predicting the anisotropic plastic flow of Al-Li alloys of various tempers has not been developed in the literature.

The present work aims to address this gap through experimentation and modelling, in a third generation Al-Li alloy, AA2198. In the present model, the state of hardening of the slip systems is obtained as a volume weighted sum of three hardening modes: (1) matrix hardening, (2) hardening due to anisotropic precipitates, and (3) hardening due to isotropic precipitates. While hardening mode (1) encompasses contributions from solution strengthening, grain, and sub-grain strengthening, and dislocation strengthening, hardening modes (2) and (3) account for precipitation strengthening. The modelling of modes (2) and (3) reflects the qualitative understanding (Crooks et al., 1998; Deschamps et al., 2013) that in aged Al-Li alloys, precipitates, which act as obstacles to dislocation motion in the early stages of plastic flow, get sheared and gradually lose their ability to obstruct dislocation movement. The state of hardening of a grain is represented using state variables, and equations governing their evolution are proposed. A simple relationship between the mechanical stretching before ageing, and the density of precipitates in the aged material is also proposed.

Table 1: Chemical composition of the present AA 2198 alloy, in weight-%, according to the manufacturer’s specification.

Si	Fe	Cu	Mg	Mn	Zn	Ti
0.08	0.10	2.90–3.50	0.25–0.80	0.50	0.35	0.10
	Zr	Ag	Li	Al		
	0.04–0.18	0.10–0.50	0.80–1.10	balance		

2. Experimental

The alloy used in the present study is a third generation Al-Cu-Li-Mg-Zr alloy (AA2198) processed by M/s ConstelliumTM with chemical composition listed in Table 1. It is supplied in the form of a 2 mm thick sheet in the T8 temper condition. This temper condition is hereafter referred to as the peak aged (PA) temper. The generic processing steps involved in the production of such sheets have been described by Rioja and Liu (2012, Fig. 3). Material fabrication involves hot rolling, solution treatment, quenching, pre-deformation, and peak ageing. Pre-deformation refers to uniaxial stretching along the rolling direction to a strain of 4%. The rolling, transverse and normal directions are henceforth denoted RD, TD, and ND, respectively.

The PA material was used as the starting material for subsequent heat treatments. To achieve the solution treated (ST) temper condition, the PA material was re-solutionised at 505°C for 45 minutes and water quenched. Ageing the ST material at 155°C for 10 hours yielded the underaged (UA) temper.

Bulk texture measurements for the aged samples were carried out by

the Schulz reflection method, using an X-ray texture goniometer with Cu K_α radiation (D8 Discover, BrukerTM). Four incomplete pole figures (0° – 85°) from the $\{111\}$, $\{200\}$, $\{220\}$ and $\{311\}$ peaks were measured at the mid-thickness section, parallel to the rolling plane. Defocussing correction of the measured data was performed using a random aluminium powder sample. The three dimensional orientation distribution function (ODF) was calculated from the measured pole figures using the free Matlab toolbox M-Tex software (Bachmann et al., 2011)

Optical microscopy on the aged specimen was performed to study the grain morphology. Samples were prepared by conventional metallographic polishing. This involved standard emery paper polishing, followed by polishing with alumina and sub-micron diamond. The polished specimens were then etched by Keller’s reagent (Nayan et al., 2013a). For transmission electron microscopy (TEM), standard 3 mm discs were prepared by twin-jet electropolishing (Samajdar et al., 1998). TEM was conducted on a FeiTM Technai20 microscope operated at 200 keV.

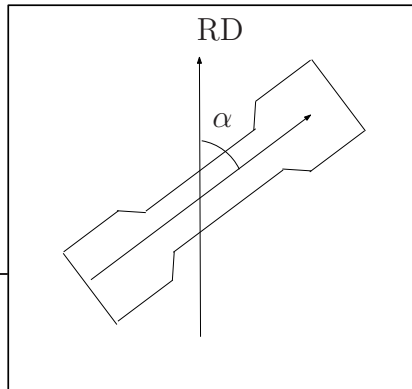


Figure 1: Tensile specimens are cut from the hot rolled plate at angles $\alpha \in \{0^\circ, 45^\circ, 90^\circ\}$.

Flat tensile samples of dimensions $110 \times 10 \times 2$ mm and gauge length 25 mm were extracted from 2 mm thick sheet at orientations of $\alpha = 0^\circ$, 45° , and 90° to the rolling direction in different temper conditions for tensile testing at ambient temperature. Tensile testing was performed in an MTS servo-hydraulic test machine operating in stroke control mode as per ASTM: E8-M-08 standard. The crosshead displacement rate was 2 mm/minute ($\sim 1.3 \times 10^{-3} \text{ s}^{-1}$). The strain measurement was done by an extensometer with 25 mm gauge length.

3. Hardening model

Strain-gradients will develop in the present material near precipitates, and near grain boundaries. It will be shown in Sec. 4.1 that the size scale of the precipitates is much smaller than that of the grains. Therefore, the hardening due to the strain gradients at the precipitates is treated in an average sense by subsuming it into the dislocation-precipitate interactions, as detailed in Sec. 3.3. Also, it will be shown in Sec. 4.1 that the present Al-Li alloy polycrystal is coarse-grained. In a coarse-grained material, the grain boundary regions contribute relatively little toward accommodating the imposed plastic deformation (Khan and Liu, 2016). Therefore, it is presently assumed that the plastic deformation of the polycrystal is accommodated by dislocation motion within the grains (Choi and Barlat, 1999). A typical grain hardens due to dislocation-dislocation (matrix hardening), and dislocation-precipitate (precipitate hardening) interactions. The present grain-level hardening model extends the classical model due to Tomé et al. (1984), which accounted only for matrix hardening in precipitate-free OFHC

copper.

3.1. Hardening modes

The model aluminium-lithium grains are assumed to deform homogeneously by $\{111\}\langle 110\rangle$ slip. Let $\dot{\gamma}_s$ denote the instantaneous slip-rate in slip system s during plastic deformation. The slip direction, and slip plane normal of this slip system are denoted \mathbf{b}_s , and \mathbf{n}_s , respectively. Then, the rate of deformation is given by (Kocks et al., 1998)

$$\mathbf{D} = \sum_{s=1}^S \mathbf{m}_s \dot{\gamma}_s. \quad (1)$$

Here, $\mathbf{m}_s = (\mathbf{b}_s \otimes \mathbf{n}_s + \mathbf{n}_s \otimes \mathbf{b}_s)/2$ denotes the Schmid tensor corresponding to the s -th slip system, and S denotes the total number of slip systems.

Hardening of slip systems in the model is described using a linear superposition of hardening modes $m \in \{1, 2, \dots, M\}$. Let the volume fraction of the grain over which hardening mode m is effective be $f^{(m)}$. While it is necessary that $f^{(m)} \leq 1$, the spatial sub-regions of the grain over which the hardening modes are effective may overlap, i.e., $\sum_{m=1}^M f^{(m)}$ may exceed unity. The critical resolved shear stress (CRSS) of the s -th slip system is taken as a weighted average of those of the modes, i.e.,

$$\tau_s = \sum_{m=1}^M f^{(m)} \tau_s^{(m)}, \quad (2)$$

where $\tau_s^{(m)}$ denotes the CRSS corresponding to the m -th mode.

$\tau_s^{(m)}$ itself is related to a state variable associated with each slip system s , and mode (m) , denoted $\Gamma_s^{(m)}$, through the extended Voce law (Tomé et al.,

1984):

$$\tau_s^{(m)}(\Gamma_s^{(m)}) = \tau_0^{(m)} + (\tau_1^{(m)} + \theta_1^{(m)}\Gamma_s^{(m)}) \left\{ 1 - \exp\left(-\frac{\Gamma_s^{(m)}\theta_0^{(m)}}{\tau_1^{(m)}}\right) \right\}. \quad (3)$$

Here, $\tau_0^{(m)}$, $\tau_1^{(m)}$, $\theta_0^{(m)}$, and $\theta_1^{(m)}$ denote material constants describing the hardening in mode m . The physical meaning of these parameters is given by Tomé et al. (1984). $\Gamma_s^{(m)}$ in Eq. (3) is termed the effective accumulated slip. Slip activity in slip system s' will affect the density of obstacles in slip system s , producing latent hardening (Kocks et al., 1998). To account for latent hardening, the effective accumulated slip, $\Gamma_s^{(m)}$, $s \in \{1, 2, \dots, S\}$ is taken to evolve following:

$$\dot{\Gamma}_s^{(m)} = \sum_{s'=1}^S g_{ss'}^{(m)} \dot{\gamma}_{s'}, \quad (4)$$

where $g_{ss'}^{(m)}$ are material constants that capture the interaction between slip systems s and s' .

The present approach to account for the interactions between slip systems differs from the classical approach (Tomé et al., 1984; Wang et al., 2013), wherein CRSS represent the internal state of a grain. Classically, CRSS evolution is taken to follow $\dot{\tau}_s = f(\Gamma) \sum_{s'} h_{ss'} \dot{\gamma}_{s'}$, where $h_{ss'}$ is a hardening matrix, and $f(\Gamma)$ is a function of the total accumulated slip in the grain. However, in the present approach, the equivalent accumulated slips $\Gamma_s^{(m)}$ are the primary internal state variables; CRSS are derived from them through Eq. (3). This approach offers greater flexibility to account for anisotropic hardening arising from both dislocation-dislocation, and dislocation-precipitate interactions, as shown below.

3.2. Initial values of the effective accumulated slip, $\Gamma_s^{(m)}$

Three hardening modes are assumed to operate in the present Al-Li grains. Mode $m = 1$ corresponds to matrix hardening, mode $m = 2$ to hardening due to dislocation interaction with anisotropic precipitates, such as T_1 , and mode $m = 3$ to dislocation interaction with isotropic precipitates, such as δ' , θ' , or Guinier-Preston (GP) zones. For each of these hardening modes, $\Gamma_s^{(m)}$ is initialised to reflect the presence of precipitates. These values together determine the yield strength of the material.

3.2.1. Mode 1: Initial matrix hardness

Mode (1) captures the mechanisms of hardening that do not arise from dislocation-precipitate interactions. These mechanisms include solution strengthening, grain and sub-grain strengthening, and dislocation strengthening (Starink et al., 1999). Matrix hardening takes place in the matrix of UA and PA tempers, and throughout the grain in the ST temper. The ST temper can be expected to be slightly harder than the matrix material in the UA or PA tempers, on account of the greater concentration of solute atoms in the ST temper. This difference is, however, neglected, and the matrix material in the UA and PA tempers are assumed to have the same hardness as an ST grain. The independence between matrix hardening and precipitation implies

$$\Gamma_s^{(1)} = 0, \quad \text{for all } s \in \{1, 2, \dots, S\}. \quad (5)$$

Following Eq. (3), this initialises the CRSS from mode (1) in all the slip systems to $\tau_0^{(1)}$.

3.2.2. Mode 2: Initial hardness due anisotropic precipitates

Plate-shaped T_1 precipitates are the anisotropic precipitates of present interest. Let the number density of T_1 precipitates lying parallel to the s' -th slip plane be denoted $\rho_{s'}$. Let Γ^{age} be a fitting parameter, representing the intensity of precipitation occurring during ageing. Γ_{age} is a function of ageing time and temperature. At a fixed ageing temperature, Γ_{age} will increase with ageing time up to the peak age condition wherein the material achieves its the greatest yield strength (Cassada et al., 1991a,b). Since the ageing time of the PA material is greater than that of the UA material, Γ^{age} of the former must exceed that of the latter. For the ST material, $\Gamma^{\text{age}} \equiv 0$.

In PA material, Cassada et al. (1991a,b) have shown that during age-hardening, plate-shaped T_1 precipitates preferentially nucleate at jogs in dislocation lines on $\{111\}$ crystallographic planes that were activated during prior stretching. Because re-solutionisation annihilates the dislocations stored in the active glide planes during stretching, the density of T_1 precipitates in the UA material can be expected to be much smaller than that in the PA material (Cassada et al., 1991a,b). To incorporate these experimental observations into the present model, let $\gamma_s^{\text{stretch}}$ denote the accumulated slip during the 4% uniaxial pre-deformation stretch along RD imparted to the material before age hardening (Sec. 2). Then, the total accumulated slip in the slip systems coplanar with s is

$$\Gamma_s^{\text{stretch}} = \sum_{\{s': \mathbf{n}_{s'} \cdot \mathbf{n}_s = 1\}} \gamma_{s'}^{\text{stretch}}. \quad (6)$$

The following linear dependence of $\rho_{s'}$ on $\Gamma_{s'}^{\text{stretch}}$ is proposed:

$$\rho_{s'} = \frac{\Gamma^{\text{age}} + \Gamma_{s'}^{\text{stretch}}}{\Gamma_*^{(2)}}, \quad (7)$$

where $1/\Gamma_*^{(2)}$ is a constant of proportionality, to be fit. The case that $\Gamma^{\text{age}} \ll \Gamma_{s'}^{\text{stretch}}$ corresponds to one wherein precipitation during age hardening occurs only at the defects introduced during stretching. The opposite case that $\Gamma^{\text{age}} \gg \Gamma_{s'}^{\text{stretch}}$ corresponds to precipitate nucleation occurring independent of the defect sites introduced during stretching. If, however, Γ^{age} and $\Gamma_{s'}^{\text{stretch}}$ are comparable, it indicates that precipitate nuclei form preferentially at dislocation jogs, but also elsewhere in the grain. The latter possibility was observed experimentally by Kumar et al. (1996) in well-aged material.

Plate shaped T_1 precipitates with a $\{111\}$ habit plane will not obstruct the motion of dislocations in any of the slip systems coplanar with the habit plane. More generally, the obstacle to dislocation motion in slip system s' due to T_1 precipitates parallel to the s -th slip system must be proportional to the geometric factor $|\mathbf{b}_{s'} \cdot \mathbf{n}_s|$. Therefore, the effective accumulated slip for mode (2) is initialised to:

$$\Gamma_s^{(2)} = \sum_{s'=1}^S |\mathbf{b}_s \cdot \mathbf{n}_{s'}| \rho_{s'} = \sum_{s'=1}^S |\mathbf{b}_s \cdot \mathbf{n}_{s'}| \left(\frac{\Gamma_{s'}^{\text{stretch}} + \Gamma^{\text{age}}}{\Gamma_*^{(2)}} \right), \forall s \in \{1, 2, \dots, S\}. \quad (8)$$

3.2.3. Mode 3: Initial hardness due to isotropic precipitates

The role of prior plastic deformation during stretching on the nucleation of isotropic precipitates, such as the spherical δ' precipitate, is not as well understood as that of T_1 precipitates. For simplicity, therefore, it is presently assumed that precipitation of isotropic precipitates follows the same mechanism as anisotropic precipitation, except that the anisotropic dependencies are suppressed. This is most simply realised by initialising the effective ac-

cumulated slip for the isotropic hardening mode following Eq. (8) to

$$\Gamma_s^{(3)} = \sum_{s'=1}^S \left(\frac{\Gamma^{\text{age}} + \Gamma_{s'}^{\text{stretch}}}{\Gamma_*^{(3)}} \right), \forall s \in \{1, 2, \dots, S\}. \quad (9)$$

Here, $\Gamma_*^{(3)}$ in Eq. (9) is a fitting parameter. It follows from Eq. (9) that $\Gamma_s^{(3)}$ is identical for all s .

3.3. Hardening during plastic deformation

The hardening matrix $g_{ss'}^{(m)}$ in Eq. (4) determines the hardening interactions between slip systems during plastic deformation. For simplicity, slip systems in hardening modes (1) and (3) are assumed not to interact. The self-hardening of these slip systems is represented as:

$$g_{ss'}^{(1)} = \begin{cases} K^{(1)}, & \text{if } s = s', \\ 0, & \text{if } s \neq s', \end{cases} \quad (10)$$

and

$$g_{ss'}^{(3)} = \begin{cases} K^{(3)}, & \text{if } s = s', \\ 0, & \text{if } s \neq s', \end{cases} \quad (11)$$

for constant $K^{(1)}$, and $K^{(2)}$, to be fit.

The hardening matrix for the anisotropic hardening mode (2) is, however, more complex. This is because the plate-shaped T_1 precipitates act as effective obstacles to dislocation motion at the beginning of plastic deformation. In this regime, the dislocations piled up at the precipitates exert back-stress on the slip systems, thereby hardening them. The magnitude of the back-stress depends on the angle between the slip direction, \mathbf{b}_s , and the normal

to the habit plane of the precipitate, $\mathbf{n}_{s'}$. The back-stress is modelled as an increase in the effective precipitate density, $\rho_{s'}$ (Eq. (7)), as:

$$\dot{\rho}_{s'} = K^{(2)} \sum_{s=1}^S |\mathbf{n}_{s'} \cdot \mathbf{b}_s| \dot{\gamma}_s, \quad (12)$$

where, $K^{(2)}$ is a parameter. Time differentiating Eq. (8), which describes the dependence of the effective accumulated slip in slip system s , on $\rho_{s'}$ yields:

$$\dot{\Gamma}_s^{(2)} = \sum_{s'=1}^S |\mathbf{b}_s \cdot \mathbf{n}_{s'}| \dot{\rho}_{s'}. \quad (13)$$

Substituting Eq. (12) into Eq. (13),

$$\dot{\Gamma}_s^{(2)} = K^{(2)} \sum_{s'=1}^S \sum_{s''=1}^S |\mathbf{b}_s \cdot \mathbf{n}_{s'}| |\mathbf{b}_{s'} \cdot \mathbf{n}_{s''}| \dot{\gamma}_{s'}, \quad (14)$$

and finally, comparing Eqs. (4) and (14) reveals that

$$g_{ss'}^{(2)} = K^{(2)} \sum_{s''=1}^S |\mathbf{b}_s \cdot \mathbf{n}_{s''}| |\mathbf{b}_{s'} \cdot \mathbf{n}_{s''}|. \quad (15)$$

The hardening coefficients, $g_{ss'}^{(m)}$, $m = 1, 2$, and 3, have been assigned particularly simple forms. The actual interaction between slip systems will be more complex. For example, in single phase fcc crystals, Franciosi and Zaoui (1982), Madec et al. (2003), and Gérard et al. (2013) have shown that junctions of widely varying strength are formed by dislocations associated with different slip system pairs. Determining these parameters systematically requires a number of latent hardening tests on single crystals (Franciosi et al., 1980), or dislocation dynamics simulations (Madec et al., 2003). As the latent hardening ratios for the present material are not presently available, and the available monotonic tensile test data does not offer sufficient constraint to

determine the individual elements of $g_{ss'}^{(m)}$, $m = 1, 2$, and 3 , these hardening matrices are assigned the simplest possible forms, reflecting only geometric considerations. Also, following Tomé et al. (1984), the hardening interactions between different slip systems is presently assumed to be independent of accumulated plastic strain. While more complex hardening interactions, summarised by Busso and Cailletaud (2005), have been proposed, the strain-invariant interactions are considered adequate, as the ductility of the present material in the PA temper is small. The present interaction matrices are also symmetric: $g_{ss'}^{(m)} = g_{s's}^{(m)}$, for all m , as required by the crystallographic equivalence of slip systems (Franciosi and Zaoui, 1982).

With increasing plastic deformation, the dislocations shear the precipitates they impinge upon (Csontos and Starke, 2005; Deschamps et al., 2013). The shearing reduces the obstacle posed by the precipitate to dislocation glide. However, precipitates that do not intersect the active slip systems are left undisturbed (Crooks et al., 1998). The softening that accompanies precipitate shearing will be accounted for by selecting the extended Voce hardening parameters for mode (2) appropriately.

4. Results

4.1. Microstructure

Fig. 2 shows a pseudo three-dimensional (3D) optical micrograph of 2 mm thick sheet in PA (peak aged) condition. Large pan-cake shaped grains were observed in the longitudinal-transverse (RD-TD) plane. Elongated grain structures, on the other hand, were seen in the RD-ND and TD-ND planes. The grain sizes, as measured by the standard linear intercept method, were

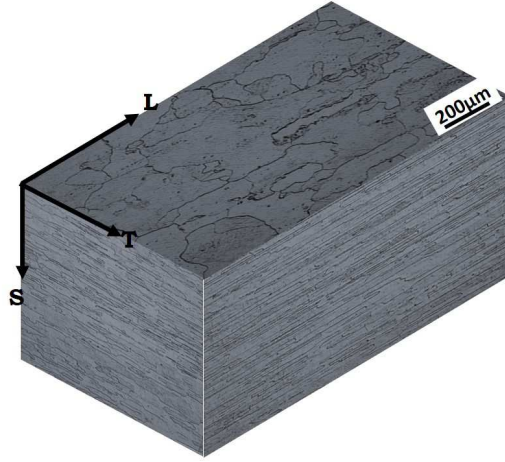
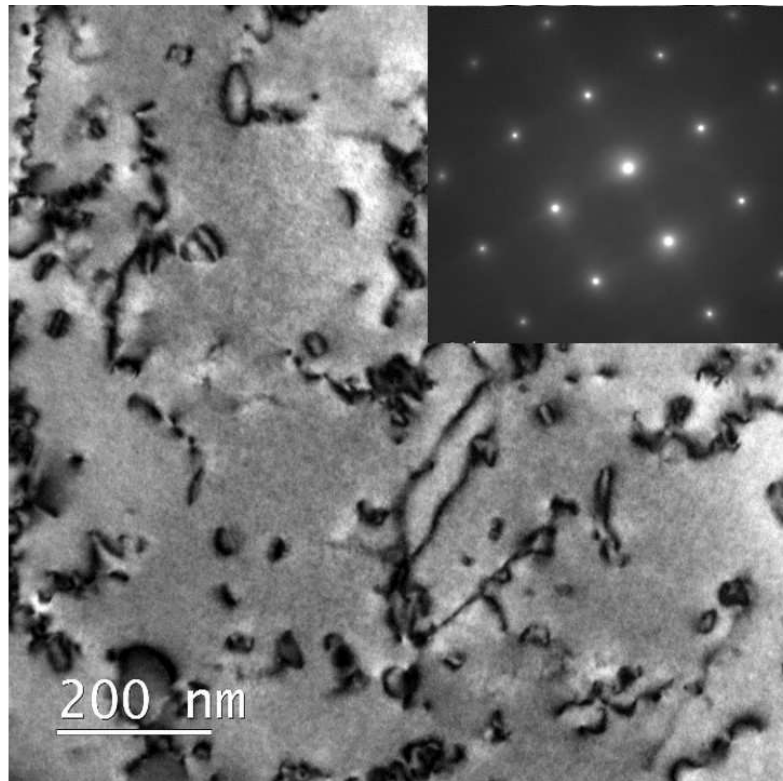


Figure 2: Pseudo-3D optical micrographs of AA2198-T8 in the peak aged (PA) temper condition. The three micrographs depict the TS, LS, and LT planes. L (longitudinal), T (transverse), and S (short transverse) directions are aligned with RD, TD, and ND, respectively.

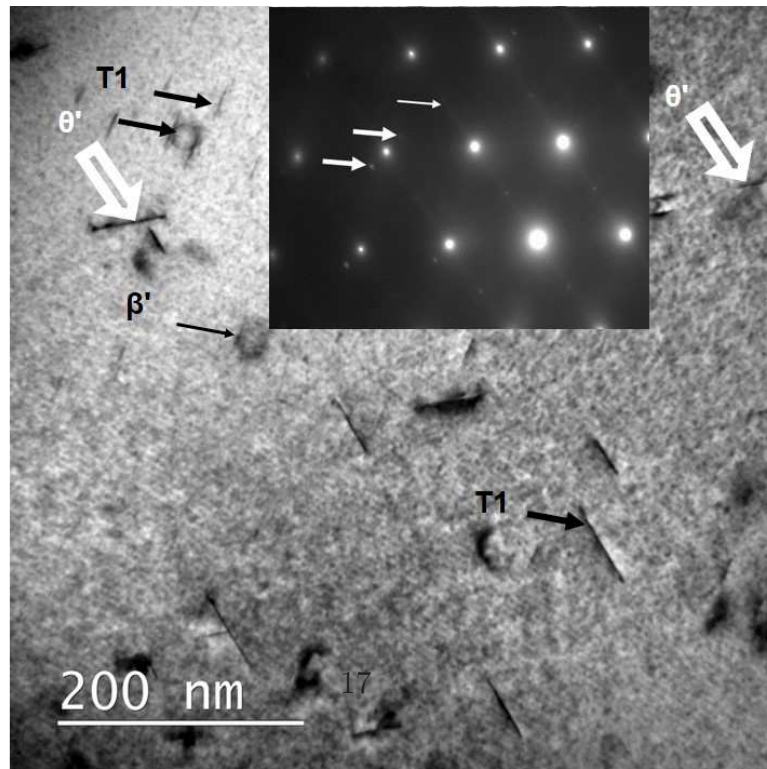
250–300 μm along RD, 50–60 μm along TD and 30–35 μm along ND. These dimensions are consistent with those reported by Le Jolu et al. (2014) in their material, which is compositionally identical to the present material.

As precipitates, and their morphology play an important role in the plasticity of the present material (Nayan et al., 2013b; Deschamps et al., 2013; Araullo-Peters et al., 2014), they have been characterised using transmission electron microscopy (TEM). Precipitates are identified through selected area electron diffraction (SAED), taken at three different zone axes: $\langle 100 \rangle_{\text{Al}}$, $\langle 110 \rangle_{\text{Al}}$ and $\langle 112 \rangle_{\text{Al}}$. The observations are summarised in Fig. 3.

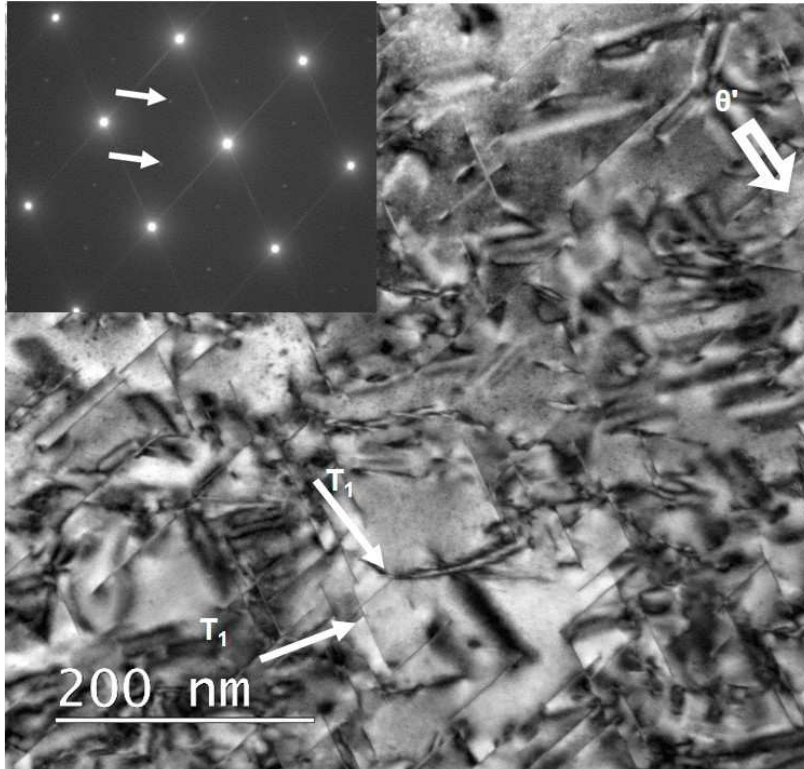
SAED in all the temper conditions reveals a spot of weak intensity corresponding to the L1_2 phase. Although this may arise from either the β' (Al_3Zr) or the δ' (Al_3Li) phases, the weakness of the intensity suggests that



(a) ST



(b) UA



(c) PA

Figure 3: Bright field transmission electron micrographs of the (a) ST temper condition along the $\langle 100 \rangle_{\text{Al}}$ zone axis, (b) UA temper along the $\langle 110 \rangle_{\text{Al}}$ zone axis, and (c) PA temper along the $\langle 112 \rangle_{\text{Al}}$ zone axis. Selected area diffraction patterns (SADP) are also included in the respective insets. Arrows point to the different types of precipitates observed.

it corresponds to β' dispersoids (Deschamps et al., 2017). The presence of dislocation loops and helices in the solution treated samples (Fig. 3a) implies that the vacancies are not permanently bound to lithium and magnesium atoms in the solid solution. The free vacancies are therefore, available at certain sites to condense into dislocation loops and/or to form helices (Gregson et al., 1986). This also implies that the presence of lithium at this concentration could not inhibit the formation of G-P zones in the Al-Cu and G-P-B zone in the Al-Cu-Mg system due to non-availability of free vacancies. Such an interpretation is consistent with the mottled appearance of the solution treated microstructure and the presence of streaks along the $\langle 001 \rangle_{\text{Al}}$ orientations. It has to be considered that the G-P zone and the G-P-B zone cause the appearance of the streaks along $\langle 001 \rangle_{\text{Al}}$ orientation in SAEDP.

Fig. 3b shows a transmission electron micrograph obtained in the $\langle 110 \rangle_{\text{Al}}$ direction showing the microstructure developed in the underaged (UA) condition of the alloy. As noted in Sec. 2, this condition was developed without any cold work prior to artificial aging. Because of the absence of stretching, heterogeneous nucleation of θ' or T_1 phase on dislocation is rarely observed. On the other hand, the close association of θ' plates with the β' dispersoids suggest that the θ' precipitates nucleate upon the β' . The nucleation of T_1 phases in UA temper condition on some the β' phase can also be seen in Fig. 3b, and is indicated by a single thick arrow. The observation of θ' phase has multiple source of nucleation in the matrix. In the underaged condition, the microstructure appears more discrete compared to the mottled appearance of the microstructure in the solution treated condition. A uniform distribution of ‘dark spots’ can be observed throughout the microstructure. These

features are consistent with the presence of G-P-B zone in the constituent Al-Cu-Mg system.

The bright field image of the PA temper, shown in Fig. 3c, reveals the presence of very thin T_1 (Al_2CuLi), θ' (Al_2Cu) precipitates, and G-P-B zones, highlighted by arrows in Fig. 3c. These have also been observed previously in similar alloys (Djaaboube and Thabet-Khireddine, 2012; de Geuser et al., 2008). The θ' plates were occasionally observed in the microstructure. The faint diffraction spots due to β' dispersoids may be observed and is attributed to the presence of fewer and non-uniform distribution of the β' dispersoids in the microstructure. The density of T_1 precipitates, which have a $\{111\}$ habit, is clearly greater in the PA condition than in the UA condition. In Fig. 3c, two variants of T_1 precipitate are visible. However, close examination of the SAED pattern reveals the presence of all four variants of the T_1 precipitate aligned with the four $\{111\}$ planes. Out of these four variants, two are perpendicular to the TEM foil plane causing streaks in the diffraction pattern, while the other two are equally inclined 35.3° to the TEM foil plane, causing spots in diffraction pattern. These T_1 precipitates, one unit cell thick (also called single layer) have been observed by Deschamps et al. (2013), and Dorin et al. (2014), and are reported to get sheared during plastic deformation (Howe et al., 1988; Csontos and Starke, 2000; Nie and Muddle, 2001; Csontos and Starke, 2005; Deschamps et al., 2013).

4.2. Stress-strain curves

The hardening model of Sec. 3 is incorporated in a binary-tree based rate-independent polycrystal plasticity model (Mahesh, 2010) to predict the mechanical response. Rate-independence has been shown to be a reasonable

Table 2: Hardening parameters for the three hardening modes of present interest.

hardening mode, m	$\tau_0^{(m)}$	$\tau_1^{(m)}$	$\theta_0^{(m)}$	$\theta_1^{(m)}$	$K^{(m)}$
	[MPa]	[MPa]	[MPa]	[MPa]	
mode $m = 1$ (matrix hardening)	75	130	620	-20	1.2
mode $m = 2$ (anisotropic hardening)	0	416	3250	-1100	0.05
mode $m = 3$ (isotropic hardening)	25	25	620	0	1.2

Table 3: Parameters to determine the initial weighted accumulated slip in a slip system due to precipitation, in the three tempers of present interest.

temper	Γ_{age}	$\Gamma_*^{(2)}$	$\Gamma_*^{(3)}$	volume fractions		
				$f^{(1)}$	$f^{(2)}$	$f^{(3)}$
	Sec. 3.2.2	Eq. (8)	Eq. (9)	Eq. (2)		
solution treated (ST)	–	–	–	1.0	0.0	0.0
underaged (UA)	0.005	15	37	1.0	0.0	0.5
peak-aged (PA)	0.05	15	37	0.2	0.8	0.8

assumption for quasi-static deformation at room temperature in a 2 series Al alloy (Khan and Liu, 2012). Despite its rate-independent character, the presently applied binary-tree based model is unaffected by Taylor ambiguity (Mánik and Holmedal, 2014). The present model represents the measured initial texture using a 1024-grain discretisation. These grains are taken to be the leaves of a balanced binary tree. In the model, each grain deforms to accommodate the imposed uniaxial deformation while maintaining traction and velocity continuity with another grain, across a grain boundary facet. The grain boundary facet is taken to be oriented at random. A pair of such co-deforming grains form a 2-grain sub-aggregate. Such a sub-aggregate is taken to deform while maintaining traction and velocity continuity with another 2-grain sub-aggregate. This process continues recursively up to the level of two 512-grain sub-aggregates, making up the 1024 grain model polycrystal.

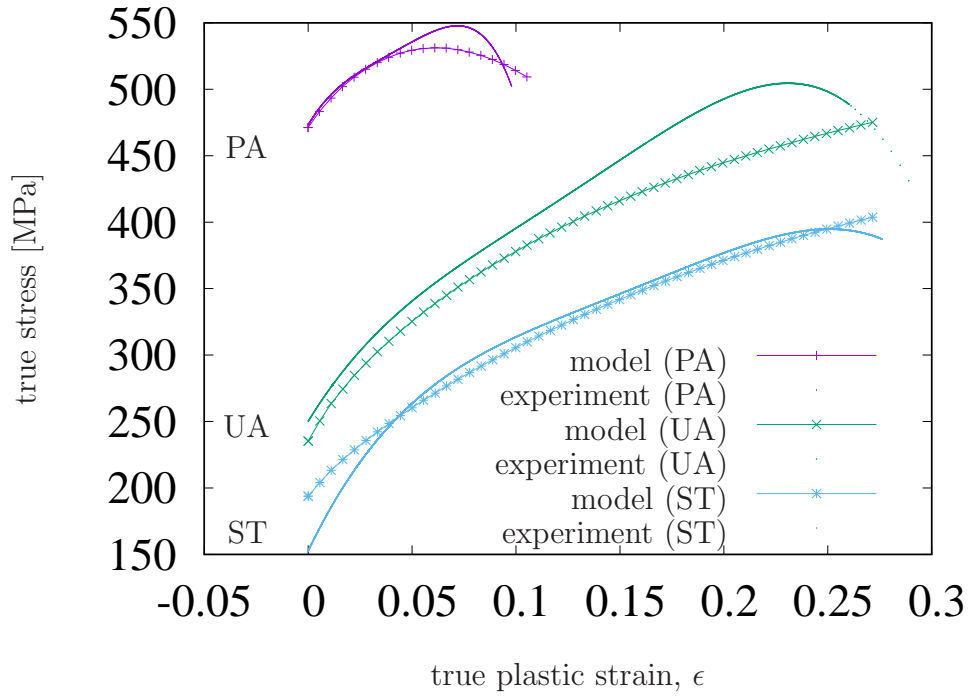
Simulation of the PA temper proceeds as follows. Pre-deformation, in the form of uniaxial stretching to 4% true strain along RD, is imposed upon the model polycrystal. The activated slip systems are identified, and $\Gamma_s^{\text{stretch}}$ is determined for each slip system s in each grain, following Eq. (6). The effective accumulated slips, $\Gamma_s^{(m)}$, for modes $m = 2, 3$, are then initialised according to Eqs. (8) and (9) to account for precipitation during ageing. Uniaxial tensile deformation along various directions α to RD is then imposed upon the polycrystal. Simulation of uniaxial tension of the UA temper proceeds similarly, except that pre-deformation stretching to 4% is skipped. This is because the effects of stretching are expected to be eliminated during re-solutionising (Sec. 2). For the ST temper, both stretching to 4% and determination of the effective accumulated slip due to ageing are skipped, as precipitates are

absent.

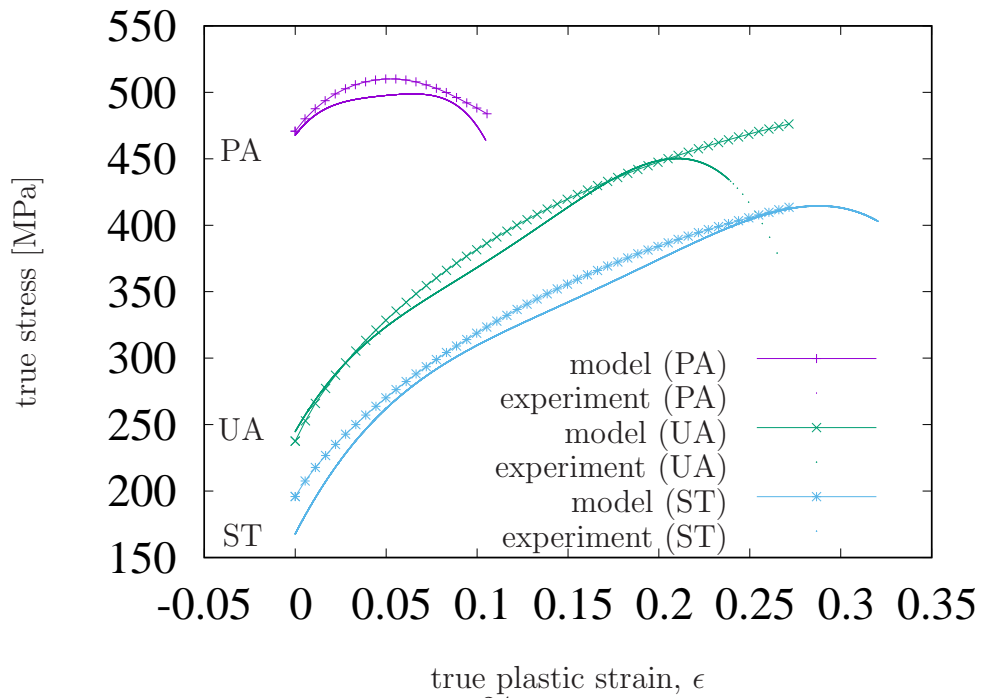
Experimentally measured true stress vs. true plastic strain curves obtained from uniaxial tensile tests performed on tensile specimen cut at $\alpha = 0^\circ$, 45° , and 90° to RD (see Fig. 1) are shown in Fig. 4. These measurements are shown for material of the ST, UA, and PA tempers. Also shown are the stress-strain curves calculated from the model, which are seen to capture the experimental measurements reasonably well. The extended Voce parameters, $\tau_0^{(m)}$, $\tau_1^{(m)}$, $\theta_0^{(m)}$, and $\theta_1^{(m)}$, and the hardening parameters $K^{(m)}$ used to obtain the model predictions are listed in Table 2. It is found that while a single mode hardening model, e.g., Tomé et al. (1984), can adequately capture the measurements in the ST temper, the present three-mode hardening model is necessary to capture the anisotropic experimental stress-strain curves for all three tempers.

The parameters, which determine the obstacle density due to precipitation at zero plastic strain in the UA and PA tempers, are listed in Table 3. Since the ST material is devoid of precipitates, these parameters are meaningless in that case, and therefore, not listed. It is found that the volume fraction for the anisotropic hardening mode, $f^{(2)}$, for the UA temper must be taken to be zero, in order to obtain the best fits with the experimental data. This suggests that the sparse distribution of the T_1 precipitates (Fig. 3b) contributes negligibly toward material hardening. The volume fractions of the anisotropic and isotropic hardening modes are comparable in the PA temper ($f^{(2)} = f^{(3)} = 0.8$).

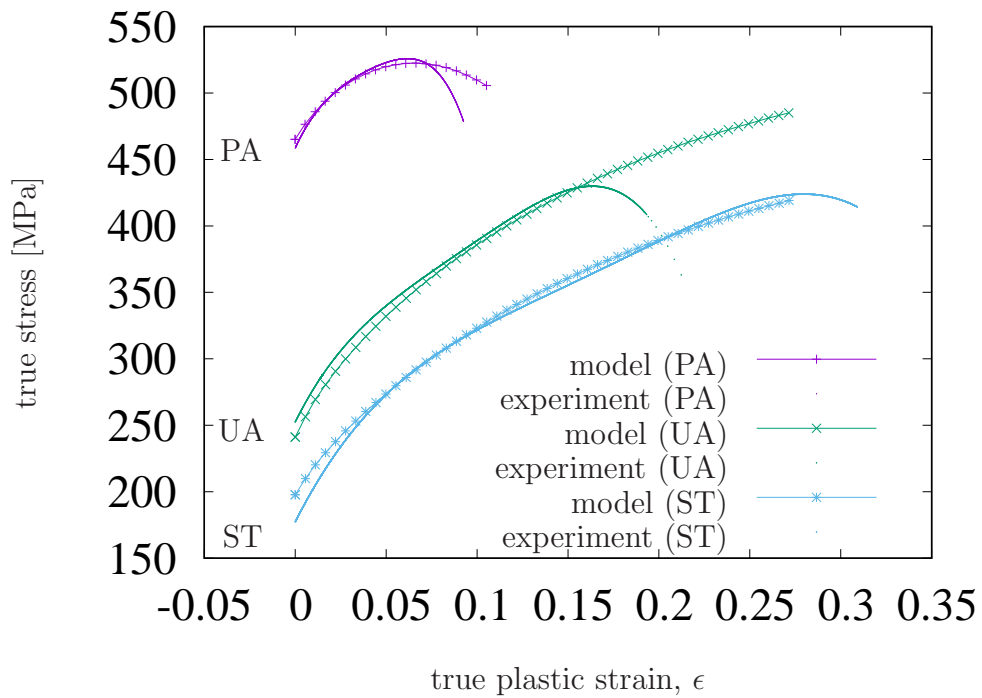
The hardening parameters listed in Table 2 can be interpreted to yield insights into the physical hardening mechanisms. While the isotropic precip-



(a) $\alpha = 0^\circ$



(b) $\alpha = 45^\circ$



(c) $\alpha = 90^\circ$

Figure 4: Comparison of the uniaxial stress-strain curves measured and predicted along (a) $\alpha = 0^\circ$, (b) $\alpha = 45^\circ$, and (c) $\alpha = 90^\circ$. In each case, flow stress evolution for the solution treated (ST), underaged (UA), and peak-aged (PA) condition are shown.

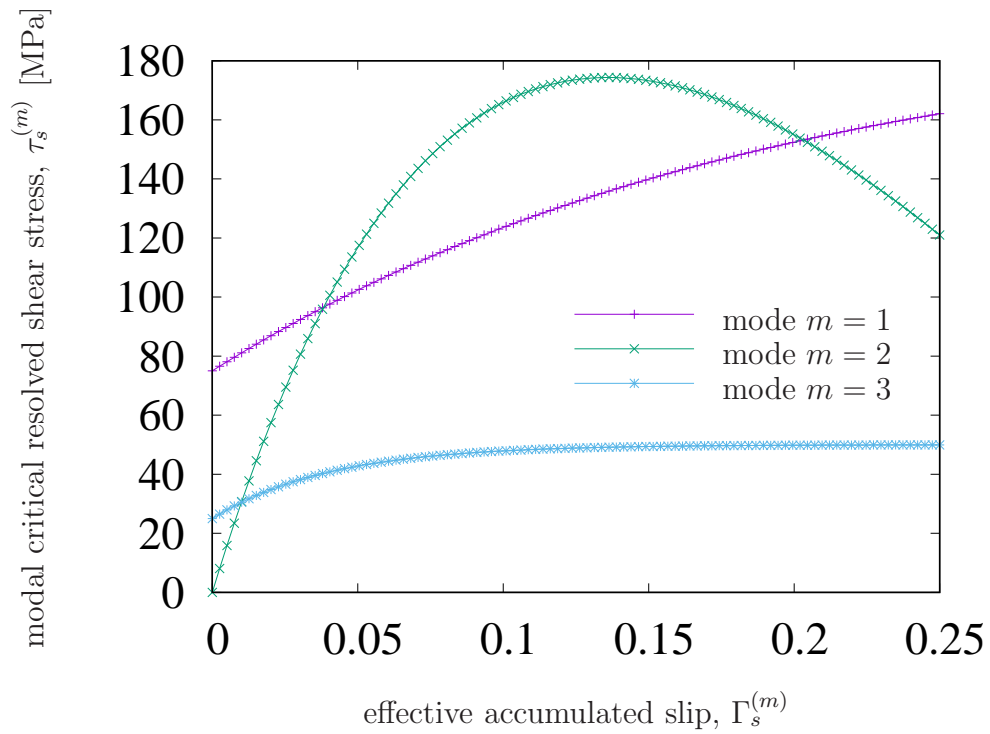


Figure 5: Evolution of the modal CRSS, $\tau_s^{(m)}$, corresponding the three hardening modes, $m = 1, 2, 3$ following Eq. (3). The hardening parameters are listed in Table 2.

itate hardening mode (3) saturates with plastic deformation, that of modes (1), and (2) decrease (soften) with $\Gamma_s^{(m)}$. In the model, this is because $\theta_1^{(1)} < 0$, and $\theta_1^{(2)} < 0$. Physically, the observed softening in mode (1) may arise from changes in the configurations of the clusters comprised of solute, micro-alloying elements, and vacancies (Sato et al., 2003) in the matrix, with strain. Physically, the observed softening in mode (2) arises from the well-known shearing of the anisotropic precipitates by slip systems impinging upon them (Crooks et al., 1998; Csontos and Starke, 2005; Deschamps et al., 2013).

The best fit Γ^{age} for the PA temper listed in Table 3 is comparable to the $\Gamma_{s'}^{\text{stretch}} \approx 0.04$ imparted to the material before age hardening. This shows that precipitation is somewhat biased toward the slip systems activated during pre-deformation (stretching). However, it is not concentrated exclusively in such slip systems. In other words, although precipitates prefer the slip planes activated during pre-deformation, they are not limited to those slip planes. This conclusion agrees with the observations of Kumar et al. (1996), based on microscopy, and with the observation of T_1 precipitates with habit planes on all the crystallographically equivalent $\{111\}$ planes in Fig. 3c.

The evolution of the CRSS in the three hardening modes with $\Gamma_s^{(m)}$, following Eq. (3), is shown in Fig. 5. The maximum contribution to CRSS comes from mode (2) (hardening due to anisotropic precipitates), and the minimum from mode (3) (hardening due to isotropic precipitates). This is consistent with the observations of Decreus et al. (2013). They found that T_1 precipitates are the dominant physical source of hardening in the present material, and that spherical δ' precipitates, which account for most of the isotropic precipitation hardening in Li-rich alloys (Gregson and Flower, 1985), are prac-

tically absent in the present AA2198 alloy. Therefore, the physical sources of isotropic hardening in the present material must be the relatively few θ' precipitates, and Guinier-Preston (GP) zones (Porter et al., 2009). This is also consistent with the microstructural observation in Figs. 3b, and 3c.

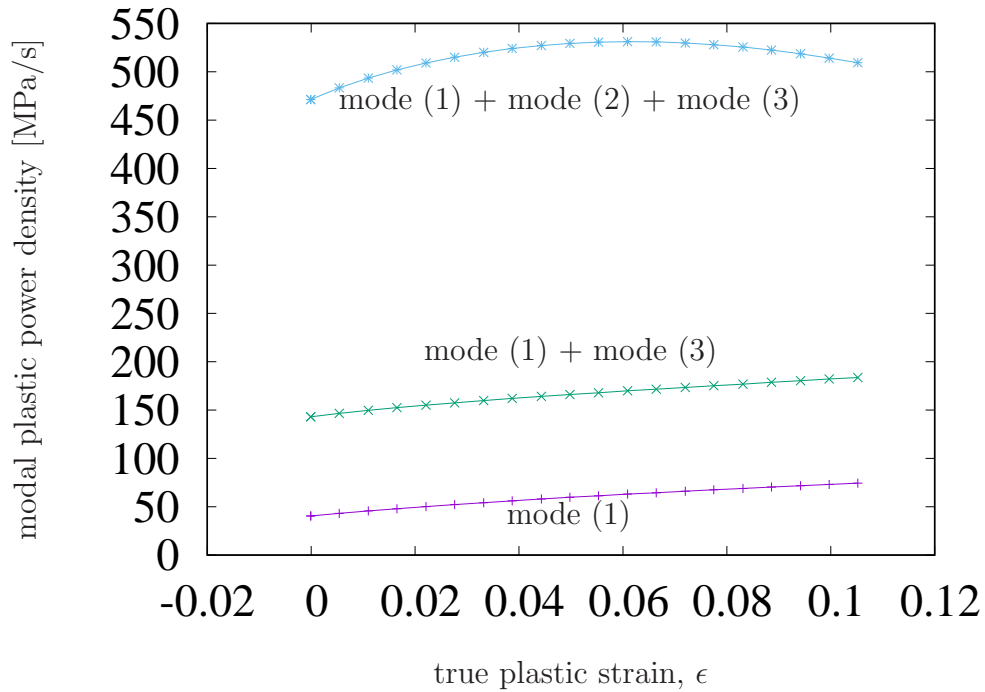


Figure 6: Calculated contributions of the three hardening modes to the plastic power density (plastic power per unit volume) dissipated by the peak-aged (PA) polycrystal in the $\alpha = 0^\circ$ specimen. Hardening modes 1, 2, and 3 represent matrix hardening, anisotropic precipitate hardening, and isotropic precipitate hardening, respectively.

The plastic power associated with the three hardening modes in the model can be used to assess their relative contributions to the macroscopic stress-strain curve in the PA temper. The variation in the plastic power associated with each of the three modes is shown in Fig. 6 for $\alpha = 0^\circ$. It is clear

that while matrix hardening (mode (1)), and isotropic precipitation hardening (mode (3)) are responsible for about a third of the hardness of the PA material, most of the material hardness arises from anisotropic precipitation hardening (mode (2)). With plastic strain, the latter contribution decreases marginally, as precipitates are sheared. Although only the case of $\alpha = 0^\circ$ is shown in Fig. 6, these observations are qualitatively valid for $\alpha = 45^\circ$, and 90° also.

4.3. Slip planarity

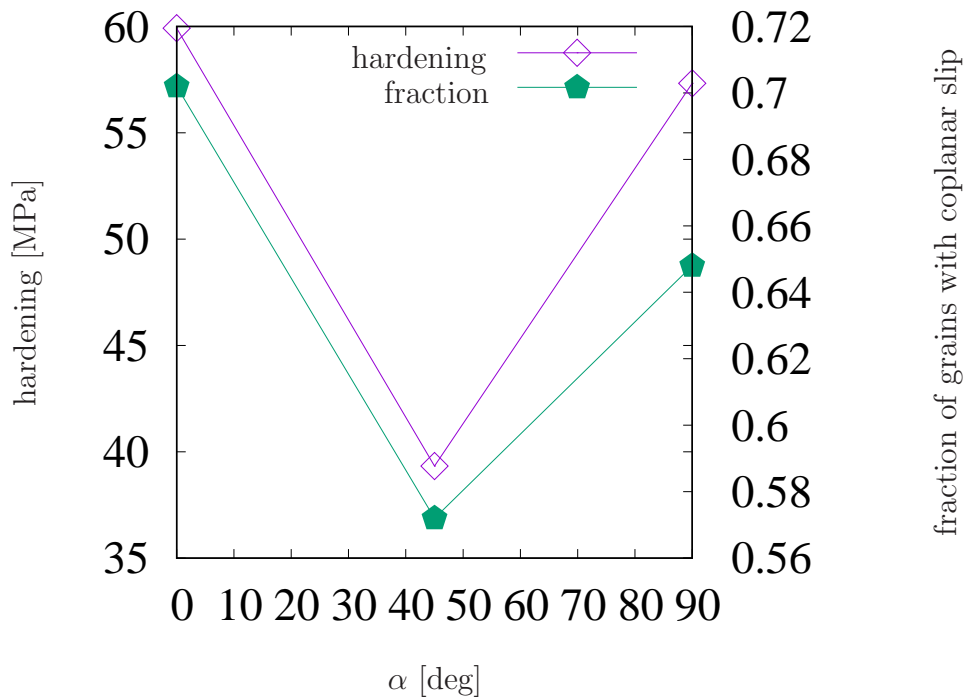


Figure 7: Model predicted hardening variation, and the fraction of grains with active coplanar slip systems, in the PA temper.

It is seen from Fig. 4 that the yield stress variation with α in the PA

temper is relatively small, compared to, e.g., the severely anisotropic AA2090 Al-Li alloy of Lee et al. (1999a). This is typical of third generation Al-Li alloys (Rioja and Liu, 2012). However, the hardening, i.e., the difference between the highest and lowest flow stresses is considerably greater for $\alpha = 0^\circ$ (75 MPa) and $\alpha = 90^\circ$ (67 MPa) than at $\alpha = 45^\circ$ (35 MPa). These values are also plotted in Fig. 7.

Two activated slip systems, s_1 , and s_2 , are coplanar if $\dot{\gamma}_{s_1} > 0$, $\dot{\gamma}_{s_2} > 0$, and $\mathbf{n}_{s_1} = \mathbf{n}_{s_2}$. The fraction of model grains with a coplanar pair of activated slip systems in the PA temper is shown in Fig. 7 for each α . A pronounced minimum is observed at $\alpha = 45^\circ$. It is clear that the fraction of grains with coplanar activated slip systems shows the same trend with α , as hardening.

To understand the similarity, consider the case $\alpha = 0^\circ$. In this case, the slip systems that are activated during pre-deformation (4% stretching) before ageing are also ideally oriented to activate during plastic deformation. According to Sec. 3.2.2, this implies that slip activity during plastic flow will occur coplanar with the preferred habit planes of the T_1 precipitates. This geometric coincidence ensures that slip activity does not try to shear the T_1 precipitates in the preferred habit plane. This causes substantially more hardening during tension along $\alpha = 0^\circ$.

The model polycrystal is subjected to macroscopic uniaxial deformation, by relaxing all the constraints in the plane transverse to the loading axis. Nevertheless, the model polycrystal undergoes nearly plane-strain deformation, i.e., the accumulated strain along ND is negligible compared to that in the RD-TD plane. On account of this, uniaxial tension along $\alpha = 90^\circ$ is approximately equivalent to uniaxial compression along $\alpha = 0^\circ$. Again,

therefore, during uniaxial tension along TD, slip activity will predominantly occur coplanar with the preferred habit planes of the $\{111\}$ T_1 precipitates, resulting in their limited shearing.

When tension is applied along $\alpha = 45^\circ$, the slip systems activated during plastic flow deviate from those activated during stretching before ageing. The geometry of slip activation is now such that T_1 precipitates in the preferred habit planes are highly likely to be sheared by the slip activity. In the model, this is the reason for the anisotropy in the hardening of the material.

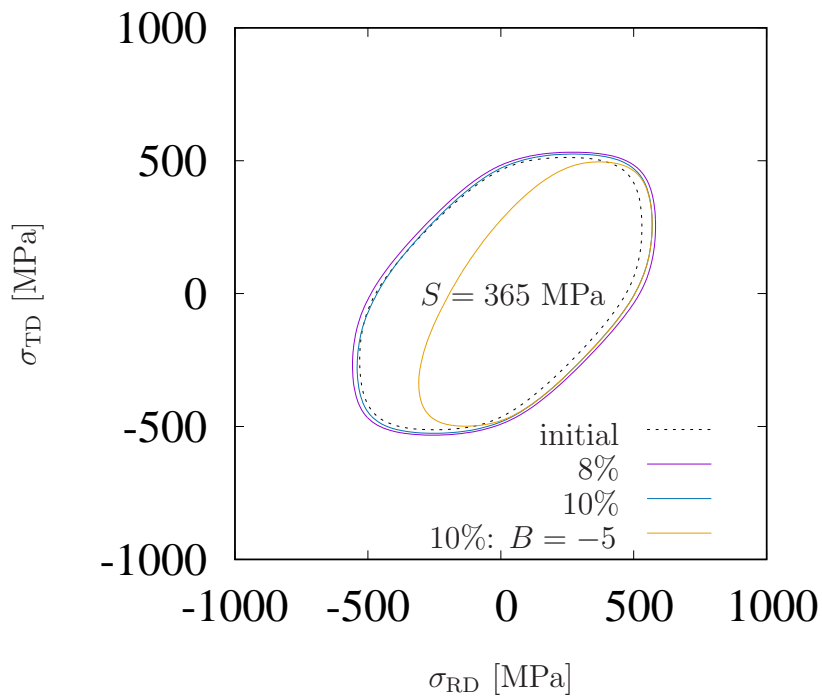
Let $\langle \Gamma_{s^*}^{(2)} \rangle$ denote the effective accumulated slip in the most active slip system s^* at the beginning of plastic deformation, averaged over all the grains. This average corresponds to the hardening mode due to anisotropic precipitates. According to the present calculation, $\langle \Gamma_{s^*}^{(2)} \rangle = 8.28 \times 10^{-2}$, 9.95×10^{-2} , and 8.90×10^{-2} , for $\alpha = 0^\circ$, 45° , and 90° , respectively. The largest $\langle \Gamma_{s^*}^{(2)} \rangle$ thus corresponds to $\alpha = 45^\circ$. The $\Gamma_s^{(2)}$ of a typical $\alpha = 45^\circ$ grain is thus closer to the peak of the $\tau_s^{(2)} - \Gamma_s^{(2)}$ curve in Fig. 5 than that of a typical $\alpha = 0^\circ$ or $\alpha = 90^\circ$ grain at the beginning of plastic deformation. The typical $\alpha = 45^\circ$ grain therefore reaches the peak at a smaller applied strain, than an $\alpha = 0^\circ$ or 90° grain, whereafter its dominant slip systems soften. This offers another rationale for why the model predicts smaller hardening at $\alpha = 45^\circ$, than at $\alpha = 0^\circ$ or $\alpha = 90^\circ$, in accord with the experimental observations.

Planar slip in Al-Li alloys takes the form of inhomogeneous grain deformation, and is known to trigger intergranular or transgranular fracture (Gregson and Flower, 1985; Csontos and Starke, 2005). A minimum plastic elongation of 5% is usually prescribed for structural components used in aerospace applications (Csontos and Starke, 2005). The elongation observed

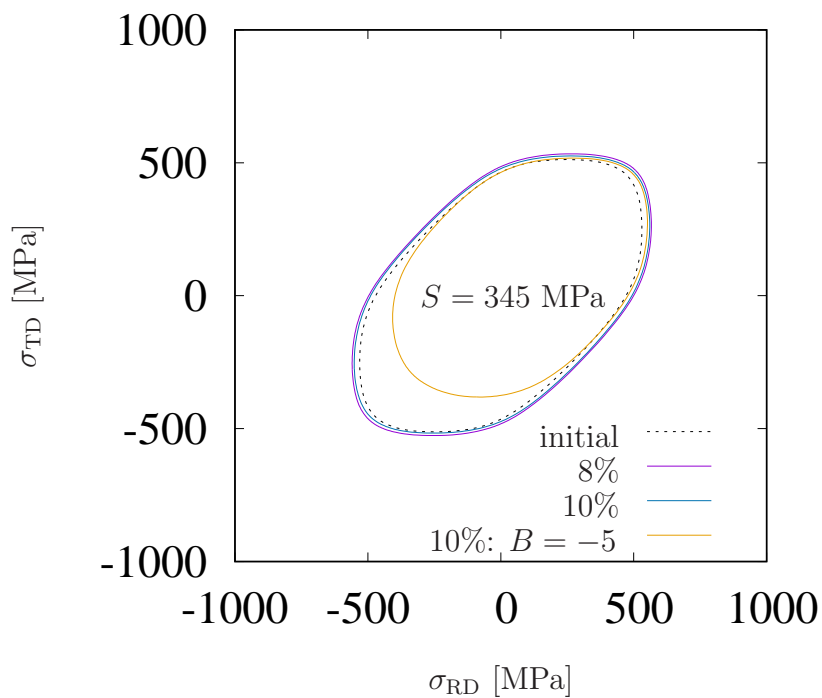
in the present PA temper material exceeds this threshold at all α . This is not because planar slip is suppressed in the present PA temper material; indeed, the present results show the opposite. Therefore, the greater elongation observed in the present material must be attributed to the nearly random texture of the present polycrystal. The nearly random texture results in a greater variety of disorientations across grain boundaries, thereby enabling them to better accommodate concentrated planar slip in the grains.

4.4. Yield surfaces

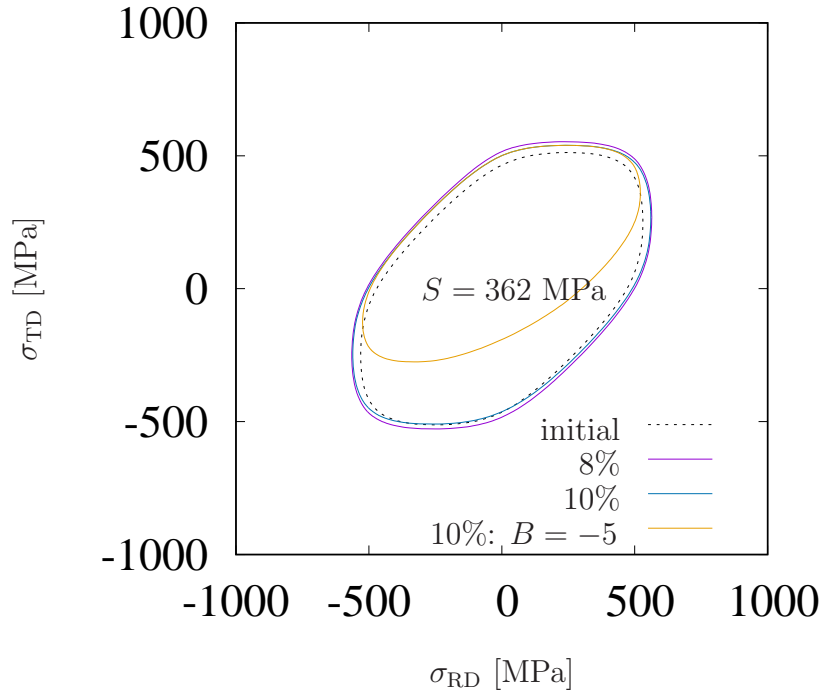
The two-component $(\sigma_{RD}, \sigma_{TD})$ yield function corresponding to biaxial stress states in the rolling plane has been calculated for the PA material, using the procedure given by Barlat and Richmond (1987). Figs. 8a, 8b, and 8c correspond to the material subjected to tension along $\alpha = 0^\circ$, 45° , and 90° , respectively. The dotted curve marked ‘initial’ is the same across the three cases, and corresponds to the predicted yield function prior to plastic deformation. The ductility of the PA material at room temperature is limited. As seen from Fig. 4, for all α , the mechanical response enters the softening regime around 8% tensile strain. In order to depict the effect of this softening, yield surfaces predicted after 8% and 10% tensile strain are plotted. Also shown in these figures is the yield strength for deformation in pure shear, $\sigma_{RD,TD} = S$, after 10% tensile strain. Comparing the yield surfaces after deformation with the initial yield surface reveals that the yield surface distorts maximally along the direction of loading. It is also seen that the yield surface predicted after 10% strain is smaller than that predicted after 8% strain. This is consistent with the softening mechanical response at 10%.



(a) $\alpha = 0^\circ$



(b) $\alpha = 45^\circ$



(c) $\alpha = 90^\circ$

Figure 8: Calculated two-component $(\sigma_{RD}, \sigma_{TD})$ yield loci of the PA specimen under biaxial loading in the RD-TD plane, before, and after plastic deformation in uniaxial tension to 8%, and 10% strain in the (a) $\alpha = 0^\circ$, (b) $\alpha = 45^\circ$, and (c) $\alpha = 90^\circ$ directions to RD. Also, the yield point for deformation in simple shear, $\sigma_{RD,TD} = S$ is shown in each case. A yield surface incorporating a hypothetical Bauschinger effect is also shown.

The predicted yield surfaces are based on the formulation of Sec. 3, and the model parameters listed in Tables 2, and 3, which in turn are obtained by fitting the monotonic flow curves in Sec. 4.2. The predicted yield surfaces possess tension-compression symmetry, i.e., if $(\sigma_{\text{RD}}, \sigma_{\text{TD}})$ lies on the yield surface, so does $(-\sigma_{\text{RD}}, -\sigma_{\text{TD}})$. In other words, the present calculations do not predict a Bauschinger effect (Lubliner, 1998).

The prediction of no Bauschinger effect is a consequence of the model parameters, which have been fitted to monotonic mechanical response measurements, and not an intrinsic limitation of the model. Tension-compression asymmetry can be predicted, for example, by taking:

$$g_{ss'}^{(m)} = Bg_{ss}^{(m)}, \quad \forall s \in \{1, 2, \dots, S\}, \quad (16)$$

if s , and s' represent opposite senses of the same slip system, i.e., $\mathbf{b}_s = -\mathbf{b}_{s'}$, and $\mathbf{n}_s = \mathbf{n}_{s'}$. Predictions obtained by setting $B = -5$, and restricting the application of Eq. (16) to mode $m = 2$ are also shown in Fig. 8. These yield surfaces are labelled ‘final: $B = -5$ ’. It is clear that a pronounced Bauschinger effect is predicted.

In Fig. 8, it is seen that one part of the ‘final’ yield surface practically coincides with that obtained by setting $B = -5$. This portion corresponds to the region wherein the slip direction in the grains predominantly coincides with that during the initial monotonic tension to 12% strain. Over the rest of the yield surface, the predominant slip direction is reversed. In this part, the ‘final’ yield surface overestimates the yield strength obtained from the $B = -5$ calculation.

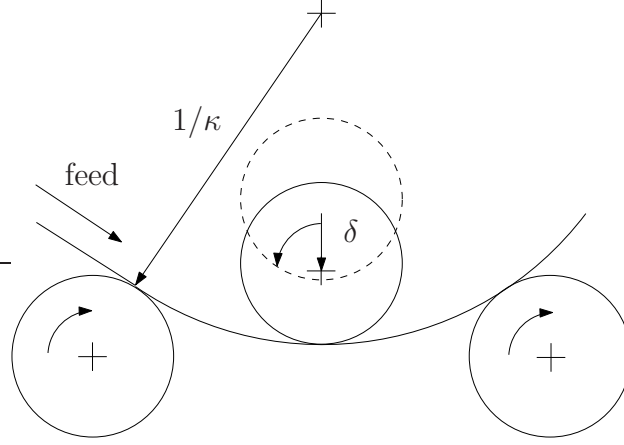


Figure 9: Schematic of the three roll bending process. The depression of the centre roll, δ , is the process input to obtain the desired curvature, κ .

4.5. Three roll bending

Three-roll bending, a process for bending plates to uniform curvature, is shown schematically in Fig. 9. The downward depression of the centre roll, δ , is the process input to obtain the desired plate curvature. δ is related kinematically to the required plate curvature, and other geometric variables, as shown by Fu et al. (2013, Eq. (2)).

The present model, calibrated to monotonic tensile tests, is adequate to model forming operations such as roll-bending, wherein, monotonic plastic deformation of material points is physically realised (Hardt et al., 1992; Fu et al., 2013). Using the elementary theory of bending, Hardt et al. (1992) expressed the relationship between the moment M applied to the plate, and its curvature, κ , as:

$$M = 2w \int_{y=0}^{t/2} \sigma(\epsilon_t(y)) y dy. \quad (17)$$

Here, $\epsilon_t(y) = \kappa y$ denotes the total bending strain, comprised of elastic and

plastic contributions, y away from the neutral axis along the thickness direction, σ the corresponding bending stress, and w the plate width.

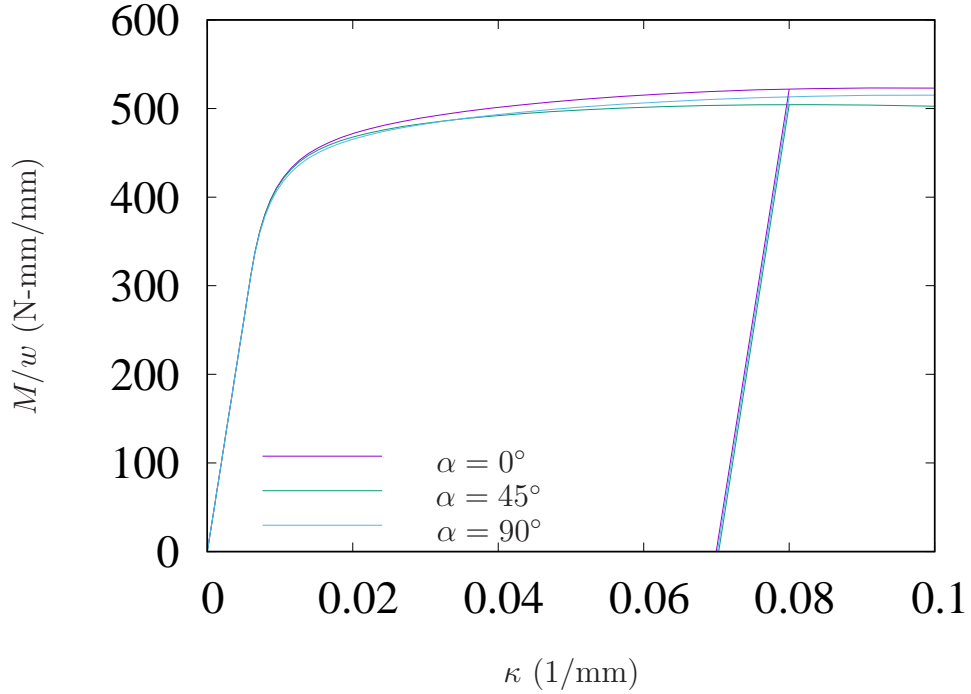


Figure 10: Moment-curvature relationship for bending a 2 mm thick plate along the three directions $\alpha = 0^\circ$, 45° , and 90° . Also shown is the nearly isotropic springback in the curvature upon unloading from $\kappa = 0.08/\text{mm}$.

The present model predicts the relationship between the true plastic strain ϵ , and stress σ (Fig. 4). Assuming the present material to be isotropically linear elastic, with Young's modulus $E = 78 \text{ GPa}$, the elastic bending strain is given by σ/E . Adding the elastic and plastic components of the bending strain leads to $\sigma(\epsilon_t(y))$ in a straightforward manner. Substituting this relationship into Eq. (17) results in the moment-curvature relationship

along $\alpha = 0^\circ$, 45° , and 90° . Fig. 10 shows the moment-curvature relationship so obtained for bending along $\alpha = 0^\circ$, 45° , and 90° . The moment-curvature diagram can be used, for example, to calculate the force exerted by the central roll on the plate (Hardt et al., 1992; Fu et al., 2013).

The bent plate will springback when unloaded. Assuming linear elastic unloading, the springback is given by $\Delta\kappa = M/(EI)$, where $I = 2w \int_{y=0}^{t/2} y^2 dy$. The springback calculated from an initial curvature of $\kappa = 0.08 \text{ mm}^{-1}$ is also shown in Fig. 10. Clearly, the springback is appreciable, but very nearly isotropic.

5. Discussion

5.1. Precipitate hardening model

Lyttle and Wert (1996) have proposed a model for the yield strength of Al-Li alloys, which also treats the precipitates as plastic inclusions. When applied to the present material, their formula becomes:

$$\sigma_y = M \left(\tau_M (1 - f_{T_1} - f_{\theta'} - f_{GP}) + f_{GP} \tau_{GP} + f_{\theta'} \tau_{\theta'} + f_{T_1} \tau_{T_1} N_{\{111\}} \right). \quad (18)$$

Here, M denotes the Taylor factor of the polycrystal; f_{T_1} , $f_{\theta'}$, and f_{GP} denote the volume fractions of the T_1 and θ' precipitates, and the GP zones, respectively; τ_M , $\tau_{\theta'}$, τ_{GP} , and τ_{T_1} denote the CRSS of the matrix, θ' precipitates, GP zones, and T_1 precipitates, respectively; and N_{111} denotes the precipitate strengthening factor, which, in turn, depends on the orientations of the $\{111\}$ habit planes of T_1 precipitates, and the polycrystalline texture (Hosford and Zeisloft, 1972).

The present model represents the flow stress as a volume weighted linear superposition of contributions from the matrix and precipitates, Eq. (2). The

form of Eq. (2) parallels that of Eq. (18). However, the scope of the present model is greater than that of Lyttle and Wert (1996). The present model predicts the flow response by capturing the microstructural evolution during plastic flow. The model of Lyttle and Wert (1996) predicts the yield stress assuming a fixed microstructure. The representation and evolution of the microstructural state in the present model have no parallels in the model of Lyttle and Wert (1996).

5.2. Texture-induced vs. precipitation-induced anisotropy

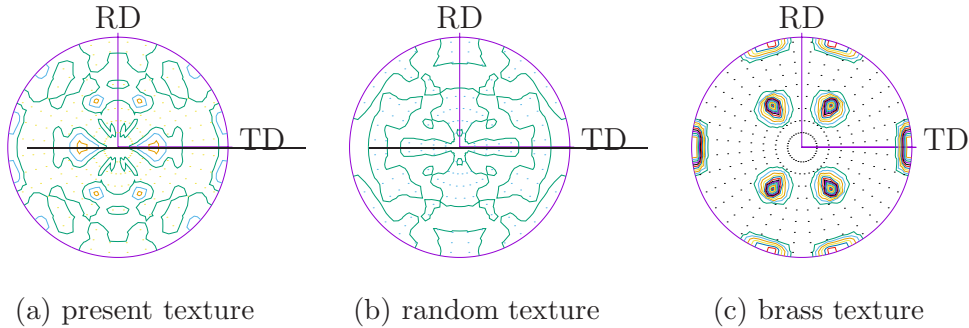
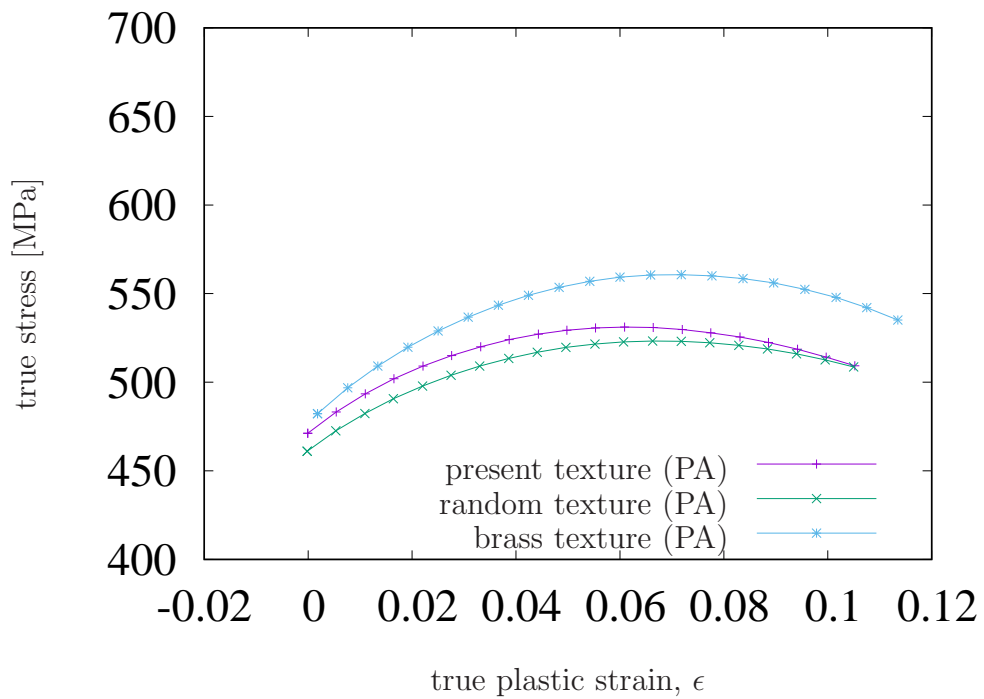
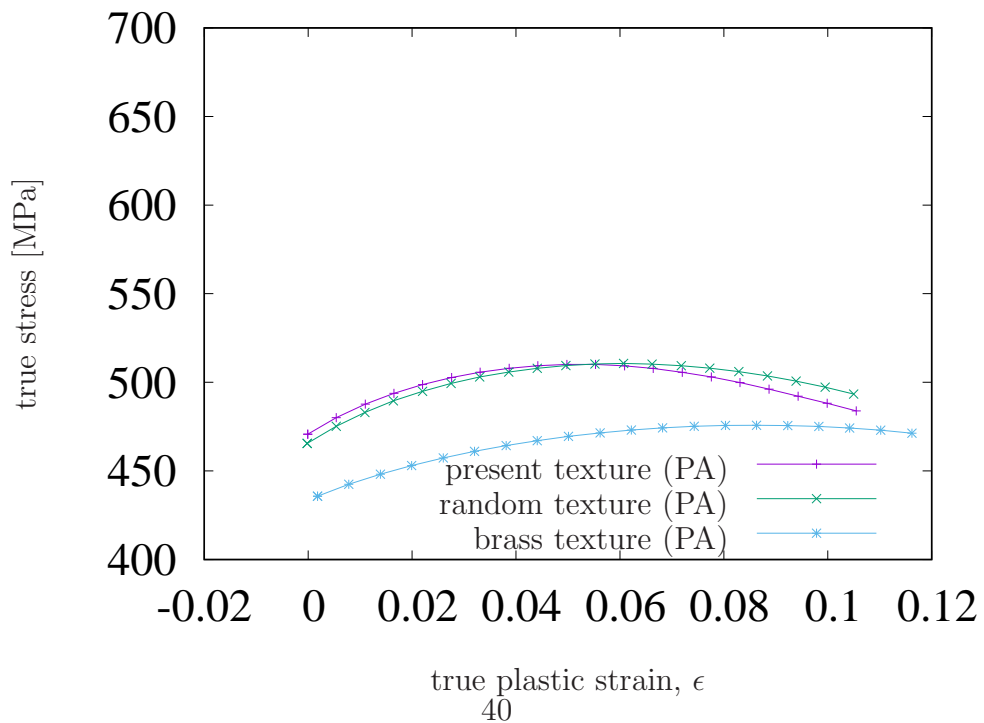


Figure 11: $\{111\}$ pole figures representing the three initial textures considered: (a) present texture, (b) random texture, and (c) brass texture. Contour levels are 1, 2, ..., 14.

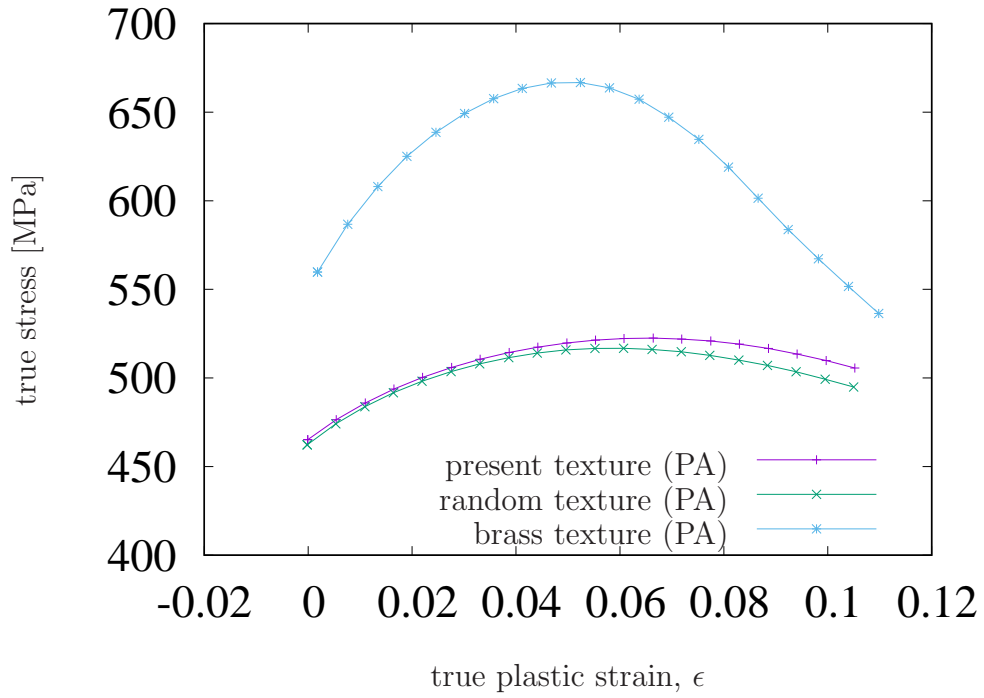
Much work in the literature (Lee and Frazier, 1988; Kim and Lee, 1993; Lee et al., 1999a; Garmestani et al., 2002) has aimed to determine the relative contributions of the crystallographic texture, and anisotropic T_1 precipitate distribution, to the anisotropy in the macroscopic plastic response. This separation is done typically by factoring out the texture contribution to the observed anisotropy by scaling by the Taylor factor. The remnant anisotropy in the yield strength scaled by the Taylor factor is attributed to anisotropy in the precipitate distributions. It must be noted that the second generation



(a) $\alpha = 0^\circ$



(b) $\alpha = 45^\circ$



(c) $\alpha = 90^\circ$

Figure 12: Comparison of uniaxial stress strain curves for the peak-aged material (PA) predicted along (a) $\alpha = 0^\circ$, (b) $\alpha = 45^\circ$, and (c) $\alpha = 90^\circ$ directions assuming the (i) measured texture of the present material, (ii) a hypothetical random texture, and (iii) a strong brass texture. The hardening model parameters are kept fixed.

Al-Li alloys, to which this procedure has been extensively applied, typically have a strong brass texture.

To quantify the contributions toward the anisotropy in the macroscopic plastic response (crystallographic texture, and anisotropic T_1 precipitate distribution among the $\{111\}$ planes), three starting textures are considered presently. They are: (i) the texture measured from the present material using X-ray diffraction, (ii) a hypothetical random texture, and (iii) a synthetic brass texture. The latter texture is comprised of grains misoriented less than 15° from the ideal brass orientation, or its sample symmetric variants. The disorientation axes are selected at random. The $\{111\}$ pole figures corresponding to these textures are shown in Fig. 11. Tensile deformation along $\alpha = 0^\circ$, 45° , and 90° is simulated starting from each of these three initial textures.

Figs. 12a, 12b, and 12c show the calculated stress-strain response for loading along $\alpha = 0^\circ$, 45° , and 90° , respectively. In all the cases, the stress-strain response predicted for the initial randomly textured polycrystal matches closely (within about 10 MPa) with that for the present texture. This suggests that the contribution of texture to anisotropy in the hardening response, is small. The observed anisotropy in hardening (Fig. 7), is therefore, almost entirely caused by the precipitate distribution with respect to the direction of loading.

The stress-strain response calculated assuming an initial brass texture deviates much more significantly from that predicted by the present texture. Most significantly, the brass textured material is harder in uniaxial tension along $\alpha = 0^\circ$, or $\alpha = 90^\circ$ than the present material. It is, however, softer than

the present material at $\alpha = 45^\circ$. Also, the softening of the brass textured material due to shearing of the precipitates is greatest for $\alpha = 0^\circ$, and 90° , while it is least for $\alpha = 45^\circ$. These observations show that in a highly textured material, the texture contribution toward anisotropy dominates the precipitate contribution.

Through polycrystal plasticity calculations, Garmestani et al. (2002) established that the strong brass texture is the primary cause for the large measured anisotropy in the yield stresses. The present results show that the anisotropy carries over into hardening during plastic flow. The present results also show that in weakly textured material, anisotropy in the precipitate distribution determines the anisotropy of the flow response.

5.3. Limitations

The present model has a number of limitations. For simplicity, and for providing adequate constraint to fit the parameters of the model, a number of simplifying assumptions have been made. For example, the ST material and the matrix material in the PA or UA tempers are assumed to be identical, even though the former can be expected to have greater solution strengthening. Only self-hardening is accounted for in modelling the hardening response of dislocation hardening, and hardening due to isotropic precipitates. These assumptions are regarded as acceptable in the present work, because (i) the present focus is on explaining the plastic response under monotonic loading, and (ii) the dislocation and isotropic hardening modes have relatively small contributions to the flow stress, compared to the dislocation-anisotropic precipitate interactions.

As noted in Sec. 4.4, model parameters have been calibrated to only capture the plastic response under monotonic loading. Model parameters relating to non-monotonic loading have been assigned zero values. A substantial Bauschinger effect, arising from directional asymmetry in the CRSS of slip systems, has been noted in Al alloys (Feigenbaum and Dafalias, 2007; Khan et al., 2009, 2010). Appropriate parameters that can capture the mechanical response during load path change tests have not been determined presently; this is left to future work.

In the literature, dislocation density based models capable of predicting the plastic response under non-monotonic strain paths have been developed, albeit only for single phase precipitate-free materials, e.g., (Peeters et al., 2001; Mahesh et al., 2004). Dislocation density based models are typically more complex than phenomenological models. In the dislocation density-based approach, non-polar, and polar dislocation densities associated with each slip system, are evolved, while accounting for their interactions. A large number of parameters must be introduced to account for the generation, annihilation, and interactions of dislocations. In these models, populations of polar dislocations, piled up at obstacles, can glide at a smaller resolved shear stress against the loading direction, than along it, to yield a macroscopic Bauschinger effect.

It seems plausible to extend the dislocation density based models to account for the precipitates, by additionally accounting for the interactions between dislocations and precipitates. This will, however, increase the number of model parameters many-fold. Assigning values to these parameters based on physical grounds will likely prove to be highly challenging, as macroscopic

mechanical tests alone are unlikely to sufficiently constrain their values. In this setting, the present phenomenological approach may be preferable as it needs only a small number of phenomenological variables.

6. Conclusion

A grain-level hardening model, which is based on, and accounts for microscopic observations of the effect of precipitates is developed, and validated against macroscopic monotonic tensile tests. Important novel features of this model are:

1. Hardening of the anisotropic precipitate hardened material has been decomposed into contributions arising from the mechanisms of matrix hardening, hardening due to anisotropic precipitates, and hardening due to isotropic precipitates;
2. Model parameters corresponding to the three mechanisms are identified independently from the macroscopic stress-strain curves for three tempers;
3. Stress-strain responses predicted by the three mechanisms are synthesised additively to obtain the stress-strain response predictions for the technologically important peak-aged temper. These predictions compare well with experimental measurements;
4. The effect of prior plasticity, and ageing treatments is accounted for, to obtain the anisotropic distribution of precipitates amongst the crystallographically equivalent $\{111\}$ habit planes. This distribution is represented in the model using an effective accumulated slip.

It is expected that the hardening framework proposed here will also be applicable to other anisotropic precipitation hardened alloys, endowed with the appropriate material-specific hardening parameters.

The model yields the following micro-scale insights into the role of the precipitates in hardening:

1. Anisotropic T_1 precipitates contribute the most to the hardening of the present Al-Li material.
2. T_1 precipitates preferentially align with $\{111\}$ planes activated during plastic deformation that precedes ageing. However, the T_1 precipitates are not exclusively concentrated in those planes.
3. Anisotropy of the precipitate distribution is the primary cause of anisotropic hardening in the present weakly textured Al-Li material.
4. Considerable hardening occurs when the activated slip systems during plastic deformation lie coplanar with the habit planes of the dominant T_1 precipitates. Contrarily, hardening is very limited if the activated slip systems intersect the habit planes of the dominant T_1 precipitates at large angles.
5. Precipitate shearing occurs when active slip systems impinge upon T_1 precipitates. Shearing occurs only after the plastic strain accumulated in a grain exceeds a certain threshold. Widespread precipitate shearing results in a softening mechanical response.

7. Acknowledgements

The authors gratefully acknowledge use of the High Performance Computing Environment at the P. G. Senapathy Centre for Computing Resources,

IIT Madras, for conducting the simulations reported in this work.

Araullo-Peters, V., Gault, B., De Geuser, F., Deschamps, A., Cairney, J. M., 2014. Microstructural evolution during ageing of al-cu-li-x alloys. *Acta Mater* 66, 199–208.

Ardell, A., 1985. Precipitation hardening. *Metall Trans A* 16 (12), 2131–2165.

Bachmann, F., Hielscher, R., Schaeben, H., 2011. Grain detection from 2d and 3d EBSD data: Specification of the MTEX algorithm. *Ultramicroscopy* 111 (12), 1720–1733.

Barlat, F., Brem, J., Yoon, J. W., Chung, K., Dick, R., Lege, D., Pourboghrat, F., Choi, S.-H., Chu, E., 2003. Plane stress yield function for aluminum alloy sheets. Part 1: theory. *Int J Plasticity* 19 (9), 1297–1319.

Barlat, F., Richmond, O., 1987. Prediction of tricomponent plane stress yield surfaces and associated flow and failure behavior of strongly textured fcc polycrystalline sheets. *Mater Sci Eng* 95, 15–29.

Busso, E. P., Cailletaud, G., 2005. On the selection of active slip systems in crystal plasticity. *Int J Plasticity* 21 (11), 2212–2231.

Campbell Jr, F., 2011. *Manufacturing technology for aerospace structural materials*. Elsevier.

Cassada, W., Shiflet, G., Starke, E., 1991a. The effect of plastic deformation on Al_2CuLi (T_1) precipitation. *Metall Trans A* 22 (2), 299–306.

Cassada, W., Shiflet, G., Starke, E., 1991b. Mechanism of Al_2CuLi (T_1) nucleation and growth. *Metall Trans A* 22 (2), 287–297.

- Choi, S., Barlat, F., Liu, J., 2001. Effect of precipitates on plastic anisotropy for polycrystalline aluminum alloys. *Metall Mater Trans A* 32 (9), 2239.
- Choi, S.-H., Barlat, F., 1999. Prediction of macroscopic anisotropy in rolled aluminum-lithium sheet. *Scripta Mater* 41 (9), 981 – 987.
- Crooks, R., Wang, Z., Levit, V., Shenoy, R., 1998. Microtexture, micro structure and plastic anisotropy of AA2195. *Mater Sci Eng A* 257 (1), 145–152.
- Csontos, A., Starke, E., 2000. The effect of processing and microstructure development on the slip and fracture behavior of the 2.1 wt pct li af/c-489 and 1.8 wt pct li af/c-458 al-li-cu-x alloys. *Metall Mater Trans A* 31 (8), 1965–1976.
- Csontos, A. A., Starke, E. A., 2005. The effect of inhomogeneous plastic deformation on the ductility and fracture behavior of age hardenable aluminum alloys. *Int J Plasticity* 21 (6), 1097–1118.
- Cyr, E. D., Brahme, A., Mohammadi, M., Mishra, R. K., Inal, K., 2018. A new crystal plasticity framework to simulate the large strain behaviour of aluminum alloys at warm temperatures. *Mater Sci Eng A* 727, 11–28.
- de Geuser, F., Gault, B., Weyland, M., Bourgeois, L., Gable, B., Ringer, S., Muddle, B., 2008. Atom probe tomography and transmission electron microscopy study of T₁ and O precipitation in an Al-Li-Cu-Mg-Ag. In: Hirsch, J., Skrotzki, B., Gottstein, G. (Eds.), *Proceedings of the International Conference on Aluminium Alloys*. Vol. 1. Wiley-VCH Verlag, pp. 724–731.

- Decreus, B., Deschamps, A., de Geuser, F., Sigli, C., 2013. Influence of natural ageing and deformation on precipitation in an Al–Cu–Li alloy. *Adv Eng Mater* 15 (11), 1082–1085.
- Deschamps, A., Decreus, B., De Geuser, F., Dorin, T., Weyland, M., 2013. The influence of precipitation on plastic deformation of Al–Cu–Li alloys. *Acta mater* 61 (11), 4010–4021.
- Deschamps, A., Garcia, M., Chevy, J., Davo, B., De Geuser, F., 2017. Influence of Mg and Li content on the microstructure evolution of Al–Cu–Li alloys during long-term ageing. *Acta Mater* 122, 32–46.
- Djaaboube, H., Thabet-Khireddine, D., 2012. TEM diffraction study of Al₂CuMg (S'/S) precipitation in an Al–Li–Cu–Mg (Zr) alloy. *Phil Mag* 92 (15), 1876–1889.
- Dorin, T., Deschamps, A., De Geuser, F., Lefebvre, W., Sigli, C., 2014. Quantitative description of the t1 formation kinetics in an Al–Cu–Li alloy using differential scanning calorimetry, small-angle x-ray scattering and transmission electron microscopy. *Philosophical magazine* 94 (10), 1012–1030.
- Feigenbaum, H. P., Dafalias, Y. F., 2007. Directional distortional hardening in metal plasticity within thermodynamics. *Int J Solids Str* 44 (22-23), 7526–7542.
- Franciosi, P., Berveiller, M., Zaoui, A., 1980. Latent hardening in copper and aluminium single crystals. *Acta metall* 28 (273–283).

- Franciosi, P., Zaoui, A., 1982. Multislip in FCC crystals: A theoretical approach compared with experimental data. *Acta metall* 30, 1627–1637.
- Fu, Z., Tian, X., Chen, W., Hu, B., Yao, X., Nov 2013. Analytical modeling and numerical simulation for three-roll bending forming of sheet metal. *Int J Adv Manuf Tech* 69 (5), 1639–1647.
- Garmestani, H., Kalidindi, S., Williams, L., Bacaltchuk, C., Fountain, C., Lee, E., Es-Said, O., 2002. Modeling the evolution of anisotropy in Al–Li alloys: application to Al–Li 2090-T8E41. *Int J Plasticity* 18 (10), 1373–1393.
- Garmestani, H., Lin, S., Adams, B. L., Ahzi, S., 2001. Statistical continuum theory for large plastic deformation of polycrystalline materials. *J Mech Phys Solids* 49 (3), 589–607.
- Gérard, C., Cailletaud, G., Bacroix, B., 2013. Modeling of latent hardening produced by complex loading paths in fcc alloys. *Int J Plasticity* 42, 194–212.
- Gregson, P., Flower, H., 1985. Microstructural control of toughness in aluminium-lithium alloys. *Acta Metall* 33 (3), 527–537.
- Gregson, P., Flower, H., Tite, C., Mukhopadhyay, A., 1986. Role of vacancies in coprecipitation of δ - and s -phases in al–li–cu–mg alloys. *Mater Sci Tech* 2 (4), 349–353.
- Hardt, D., Constantine, E., Wright, A., 1992. A model of the sequential bending process for manufacturing simulation. *J Eng Ind* 114 (2), 181–187.

- Hosford, W., Zeisloft, R., 1972. The anisotropy of age-hardened Al-4 pct Cu single crystals during plane-strain compression. *Metall Mater Trans B* 3 (1), 113–121.
- Howe, J., Lee, J., Vasudevan, A., 1988. Structure and deformation behavior of δ' precipitate plates in an Al-2Li-1 Cu alloy. *Met Trans A* 19 (12), 2911–2920.
- Huang, J., Ardell, A., 1988. Addition rules and the contribution of δ' precipitates to strengthening of aged Al–Li–Cu alloys. *Acta Metall* 36 (11), 2995–3006.
- Kabirian, F., Khan, A. S., 2015. Anisotropic yield criteria in σ – τ stress space for materials with yield asymmetry. *Int J Solids Str* 67, 116–126.
- Khan, A. S., Kazmi, R., Pandey, A., Stoughton, T., 2009. Evolution of subsequent yield surfaces and elastic constants with finite plastic deformation. Part I: A very low work hardening aluminum alloy (Al6061-T6511). *Int J Plasticity* 25 (9), 1611–1625.
- Khan, A. S., Liu, H., 2012. Variable strain rate sensitivity in an aluminum alloy: response and constitutive modeling. *Int J Plasticity* 36, 1–14.
- Khan, A. S., Liu, J., 2016. A deformation mechanism based crystal plasticity model of ultrafine-grained/nanocrystalline fcc polycrystals. *Int J Plasticity* 86, 56–69.
- Khan, A. S., Pandey, A., Stoughton, T., 2010. Evolution of subsequent yield surfaces and elastic constants with finite plastic deformation. Part II: A

- very high work hardening aluminum alloy (annealed 1100 Al). *Int J Plasticity* 26 (10), 1421–1431.
- Kim, N. J., Lee, E. W., 1993. Effect of T_1 precipitate on the anisotropy of Al–Li alloy 2090. *Acta Metall Mater* 41 (3), 941–948.
- Kocks, U. F., Tomé, C. N., Wenk, H. R., 1998. *Texture and Anisotropy*. Cambridge University Press, Cambridge, U.K.
- Kumar, K., Brown, S., Pickens, J. R., 1996. Microstructural evolution during aging of an Al–Cu–Li–Ag–Mg–Zr alloy. *Acta Mater* 44 (5), 1899–1915.
- Le Jolu, T., Morgeneyer, T. F., Denquin, A., Sennour, M., Laurent, A., Besson, J., Gourgues-Lorenzon, A.-F., 2014. Microstructural characterization of internal welding defects and their effect on the tensile behavior of FSW joints of AA2198 Al–Cu–Li alloy. *Metal Mater Trans A* 45 (12), 5531–5544.
- Lee, E., Frazier, W., 1988. The effect of stretch on the microstructure and mechanical properties of 2090 Al–Li. *Scripta Metall* 22 (1), 53–57.
- Lee, E., Kalu, P., Brandao, L., Es-Said, O., Foyos, J., Garmestani, H., 1999a. The effect of off-axis thermomechanical processing on the mechanical behavior of textured 2095 Al–Li alloy. *Mater Sci Eng A* 265 (1-2), 100–109.
- Lee, K. C., Zeng, Y. P., Lee, C. S., 1999b. Influence of external constraint on deformation banding of $\{110\}\langle uvw \rangle$ orientations. *Scripta mater.* 40 (2), 197–202.
- Lubliner, J., 1998. *Plasticity theory*. MacMillan.

- Lyttle, M., Wert, J., 1996. The plastic anisotropy of an Al–Li–Cu–Zr alloy extrusion in unidirectional deformation. *Metal Mater Trans A* 27 (11), 3503–3512.
- Madec, R., Devincere, B., Kubin, L., Hoc, T., Rodney, D., 2003. The role of collinear interaction in dislocation-induced hardening. *Science* 301 (5641), 1879–1882.
- Mahesh, S., 2010. A binary tree based model for rate-independent polycrystals. *Int J Plast.* 26 (1), 42–64.
- Mahesh, S., Tomé, C. N., McCabe, R. J., Kaschner, G. C., Beyerlein, I. J., Misra, A., 2004. Application of a sub-structure based hardening model to copper under loading path changes. *Metall Mater Trans A* 35, 3763–3774.
- Mánik, T., Holmedal, B., 2014. Review of the taylor ambiguity and the relationship between rate-independent and rate-dependent full-constraints taylor models. *Int J Plasticity* 55, 152–181.
- Mott, N., Nabarro, F., 1940. An attempt to estimate the degree of precipitation hardening, with a simple model. *Proc Phys Soc* 52 (1), 86.
- Nayan, N., Murty, S. N., Jha, A. K., Pant, B., Sharma, S., George, K. M., Sastry, G., 2013a. Processing and characterization of Al–Cu–Li alloy AA2195 undergoing scale up production through the vacuum induction melting technique. *Mater Sci Eng A* 576, 21–28.
- Nayan, N., Murty, S. N., Mukhopadhyay, A., Prasad, K., Jha, A., Pant, B., Sharma, S., George, K., 2013b. Ambient and cryogenic tensile properties

- of aa2195t87 sheets with pre-aging cold work by a combination of cold rolling and stretching. *Mater Sci Eng A* 585, 475–479.
- Nie, J., Muddle, B., 2001. On the form of the age-hardening response in high strength aluminium alloys. *Mater Sci Eng A* 319, 448–451.
- Peeters, B., Seefeldt, M., Teodosiu, C., Kalidindi, S. R., Houtte, P. V., Aernoudt, E., 2001. Work-hardening/softening behavior of bcc polycrystals during changing strain paths: I An integrated model based on substructure and texture evolution, and its prediction of the stress-strain behavior of an IF steel during two-stage strain paths. *Acta mater.* 49, 1607–1619.
- Porter, D. A., Easterling, K. E., Sherif, M., 2009. *Phase Transformations in Metals and Alloys*. CRC press.
- Rioja, R. J., Liu, J., 2012. The evolution of Al–Li base products for aerospace and space applications. *Metall Mater Trans A* 43 (9), 3325–3337.
- Rousselier, G., Barlat, F., Yoon, J. W., 2009. A novel approach for anisotropic hardening modeling. part I: Theory and its application to finite element analysis of deep drawing. *Int J Plasticity* 25 (12), 2383–2409.
- Safaei, M., Zang, S.-l., Lee, M.-G., De Waele, W., 2013. Evaluation of anisotropic constitutive models: Mixed anisotropic hardening and non-associated flow rule approach. *Int J Mech Sci* 73, 53–68.
- Samajdar, I., Ratchev, P., Verlinden, B., Van Houtte, P., De Smet, P., 1998. Dislocation cell formation and hot ductility in an al–mg–cu alloy. *Mater Sci Eng A* 247 (1-2), 58–66.

- Sato, T., Hirose, S., Hirose, K., Maeguchi, T., 2003. Roles of microalloying elements on the cluster formation in the initial stage of phase decomposition of Al-based alloys. *Metal Mater Trans A* 34 (12), 2745–2755.
- Shercliff, H., Ashby, M., 1990a. A process model for age hardening of aluminium alloys I: The model. *Acta Metall Mater* 38 (10), 1789–1802.
- Shercliff, H., Ashby, M., 1990b. A process model for age hardening of aluminium alloysii. applications of the model. *Acta Metall Mater* 38 (10), 1803–1812.
- Shi, B., Mosler, J., 2013. On the macroscopic description of yield surface evolution by means of distortional hardening models: application to magnesium. *Int J Plasticity* 44, 1–22.
- Starink, M., Wang, P., Sinclair, I., Gregson, P., 1999. Microstructure and strengthening of Al–Li–Cu–Mg alloys and MMCs: II. modelling of yield strength. *Acta Mater* 47 (14), 3855–3868.
- Tomé, C., Canova, G. R., Kocks, U. F., Christodoulou, N., Jonas, J. J., 1984. The relation between macroscopic and microscopic strain hardening in F.C.C polycrystals. *Acta metall.* 32 (10), 1637–1653.
- Vasudevan, A., Przystupa, M., Fricke Jr, W., 1990. Texture-microstructure effects in yield strength anisotropy of 2090 sheet alloy. *Scripta Metall Mater* 24 (8), 1429–1434.
- Wang, H., Wu, P., Wang, J., Tomé, C., 2013. A crystal plasticity model for hexagonal close packed crystals including twinning and de-twinning mechanisms. *Int J Plasticity* 49, 36–52.

Yoshida, F., Hamasaki, H., Uemori, T., 2015. Modeling of anisotropic hardening of sheet metals including description of the Bauschinger effect. *Int J Plasticity* 75, 170–188.